Formation of superdense hadronic matter in high energy heavy-ion collisions

Bao-An Li and Che Ming Ko
Cyclotron Institute and Physics Department, Texas A&M University, College Station, Texas 77843
(Received 10 May 1995)

We present the detail of a newly developed relativistic transport model (ART 1.0) for high energy heavy-ion collisions. Using this model, we first study the general collision dynamics between heavy ions at the AGS energies. We then show that in central collisions there exists a large volume of sufficiently long-lived superdense hadronic matter whose local baryon and energy densities exceed the critical densities for the hadronic matter to quark-gluon plasma transition. The size and lifetime of this matter are found to depend strongly on the equation of state. We also investigate the degree and time scale of thermalization as well as the radial flow during the expansion of the superdense hadronic matter. The flow velocity profile and the temperature of the hadronic matter at freeze-out are extracted. The transverse momentum and rapidity distributions of protons, pions, and kaons calculated with and without the mean field are compared with each other and also with the preliminary data from the E866/E802 Collaboration to search for experimental observables that are sensitive to the equation of state. It is found that these inclusive, single particle observables depend weakly on the equation of state. The difference between results obtained with and without the nuclear mean field is only about 20%. The baryon transverse collective flow in the reaction plane is also analyzed. It is shown that both the flow parameter and the strength of the "bounce-off" effect are very sensitive to the equation of state. In particular, a soft equation of state with a compressibility of 200 MeV results in an increase of the flow parameter by a factor of 2.5 compared to the cascade case without the mean field. This large effect makes it possible to distinguish the predictions from different theoretical models and to detect the signatures of the quark-gluon plasma which is expected to significantly soften the equation of state.

PACS number(s): 25.75.+r, 12.38.Mh, 21.65.+f, 24.85.+p

I. MOTIVATION

The main purpose of relativistic heavy-ion collisions at future RHIC and LHC energies is to create in the laboratory a quark-gluon plasma (QGP) and to study its properties. On the other hand, for heavy-ion collisions at Brookhaven's AGS the emphasis has been in studying the properties of hot dense hadronic matter and the collision dynamics. However, the possibility of a phase transition to the QGP in central heavy-ion collisions at AGS energies has also been mentioned recently.

At AGS, a vast body of data has already been collected and analyzed during the past few years [1]. Comparisons of these data with the predictions from theoretical models, such as the RQMD [2], the ARC [3], and the QGSM [4], have revealed much interesting physics. In particular, a picture of nearly complete stopping of baryons in central heavy-ion collisions has emerged from these studies. Furthermore, it has been shown that baryon and energy densities up to 10 times that in normal nuclei have been reached in these collisions, leading thus to the suggestion that in central collisions at AGS energies the QGP may have already been formed [5]. It has been further shown, based on a relativistic nucleation theory, that perhaps one in every 10^2 or 10^3 events undergoes the phase transition. However, the above suggestion and many other exotic phenomena depend crucially on the maximum energy and baryon densities reached in the collision. In this paper, we will carry out a detailed study on the formation of a superdense hadronic matter in heavy-ion collisions at AGS energies.

With the available Au beam at $p_{\rm beam}/A = 11.6$ GeV/c at AGS, more systematic study of heavy-ion collisions are being carried out by several collaboration (e.g., [6,7]). In addition, systematic and exclusive measurements of the energy and mass dependence of particle production, correlations, and collective flow effects from Bevalac energies up to AGS energies will soon be carried out by the EOS collaboration [8]. Besides studying possible new physical phenomena, these experiments will provide a broader base of data so that more stringent tests of theoretical models can be made. Also, comparisons of the experimental data with reliable model predictions will allow us to learn about the properties of hot dense hadronic matter formed in these collisions and help identify new physical phenomena. Stimulated by the success of the RQMD and the ARC in describing many available experimental data at AGS energies, we have recently developed a relativistic transport (ART) model for heavy-ion collisions at these energies. A brief report of the model has been given in Refs. [9,10]; here we will present the detail of the model (ART 1.0) and study several important aspects and issues of heavy-ion collisions at AGS energies.

More specifically, we discuss in Sec. II the details of the model ART 1.0 and its inputs. In Sec. III, we first study the general heavy-ion collision dynamics at AGS energies. We then discuss the formation of the superdense hadronic matter and its properties as well as its dependence on the equation of state. The degree of thermal equilibrium in the superdense hadronic matter and the time scale involved are also discussed. In addition, main features of the radial flow during the expansion phase, the flow velocity profile, and temperature of the hadronic matter at freeze-out are also investigated. The model is then used to study the transverse momentum and rapidity distribution of protons, pions, and kaons with and without including the mean field in order to identify

observables that are sensitive to the equation of state. These results are then compared with each other and also with the preliminary data from the E866/E802 Collaboration. Finally, we carry out a detailed analysis of the baryon transverse flow in the reaction plane and study its dependence on the equation of state. The summary and outlook are given in Sec. IV. Those interested only in the results may turn directly to Sec. III.

II. RELATIVISTIC TRANSPORT MODEL: ART 1.0

Based on the well-known Boltzmann-Uehling-Uhlenbeck (BUU) model (e.g., [11–13]) for intermediate energy heavy-ion collisions, we have recently developed a relativistic transport model for heavy-ion collisions at AGS energies [9,10] by including more baryon and meson resonances and their interactions. The BUU model has been very successful in studying heavy-ion collisions at beam energies lower than about 3 GeV/nucleon. We refer the reader to the review by Bertsch and Das Gupta for more details of the BUU model [11].

In the ART model, we have kept the same philosophy and methods as in the BUU model, but added some new physics and numerical techniques in order to simulate heavy-ion collisions at higher energies. More specifically, we have included in ART 1.0 the baryons N, $\Delta(1232)$, $N^*(1440)$, $N^*(1535)$, Λ, Σ and mesons π, ρ, ω, η, K, as well as their explicit isospin degrees of freedom. Although antiparticles and heavier mesons have so far not been included, their production can be studied perturbatively in the present version of the model. We plan to include explicitly these particles in an upgraded version of the model. Both elastic and inelastic collisions among most of these particles are included as best as we can by using as inputs the experimental data from hadron-hadron collisions. In accordance with this philosophy, almost all parametrized cross sections and angular distributions that have been used in the BUU model are replaced by empirical expressions based on the double-logarithmic interpolations of the experimental data [14]. However, more than 200 reaction channels are listed in the CERN data book [14] for nucleon-nucleon and pion-nucleon collisions. We certainly have not fully incorporated all these channels. Instead, most inelastic hadron-hadron collisions are modeled through the formation of resonances. The advantage of this approximation is that the finite lifetime of these resonances takes into account partially the effects of the finite formation time for produced secondaries. In the following, we present details of treating various hadron-hadron interactions.

A. Inelastic baryon-baryon interactions

First of all, we have included in the model the reactions

$$NN \leftrightarrow N\Delta,\ NN^*(1440),\ NN^*(1535), \tag{1}$$

$$NN \leftrightarrow \Delta\Delta,\ \Delta N^*(1440), \tag{2}$$

$$NN \rightarrow NN\rho,\ NN\omega,\ \Delta\Delta\pi, \tag{3}$$

$$NN \rightarrow \Delta\Delta\rho, \tag{4}$$

TABLE I. Isospin cross section parameters.

Parameter	σ_{11}	σ_{10}	σ_{01}
α	3.772	15.28	146.3
β	1.262	0	0
m_0(MeV)	1188	1245	1472
Γ(MeV)	99.02	137.4	26.49

$$N\Delta \leftrightarrow NN^*(1440),\ NN^*(1535), \tag{5}$$

$$\Delta\Delta \leftrightarrow NN^*(1440),\ NN^*(1535), \tag{6}$$

$$\Delta N^*(1440) \leftrightarrow NN^*(1535), \tag{7}$$

and those producing kaons as shown later in Eqs. (68)–(70). The decomposition of the total inelastic nucleon-nucleon cross section into different channels shown in the above certainly involves some uncertainties and assumptions. Moreover, most of the available data are only for the pp reaction. For the np reaction we use as much data as possible. Otherwise, we just assume that the cross sections are the same as in the pp reaction. In the following, we discuss the methods we have introduced for determining these cross sections.

As in Refs. [12,16,17], we use the parametrization introduced by VerWest and Arndt [15] for the cross sections of producing a single Δ or $N^*(1440)$ resonance in processes shown in Eq. (1). In terms of the channel isospin cross section σ_{if} with $i(f)=0$ or 1 being the initial and final isospins, the Δ and $N^*(1440)$ production cross sections are given by

$$\sigma(p+p \rightarrow n+\Delta^{++}) = \sigma_{10} + \tfrac{1}{2}\sigma_{11}, \tag{8}$$

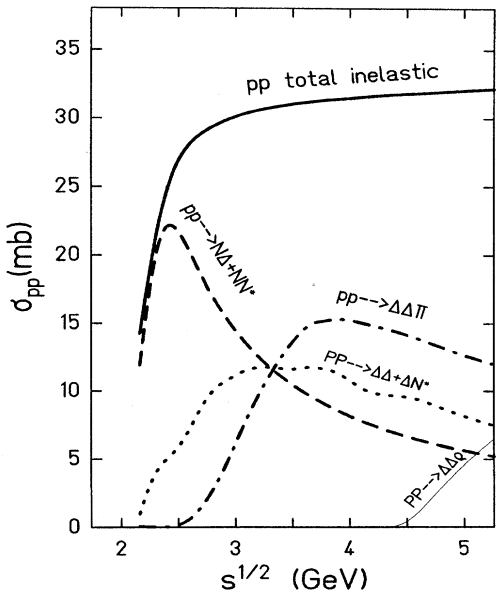

FIG. 1. pp inelastic cross sections as functions of center-of-mass energy $\sqrt{s}$.

$$\sigma(p+p\rightarrow p+\Delta^{+})=\tfrac{3}{2}\sigma_{11}, \quad (9)$$

$$\sigma(n+p\rightarrow p+\Delta^{0})=\tfrac{1}{2}\sigma_{11}+\tfrac{1}{4}\sigma_{10}, \quad (10)$$

$$\sigma(n+p\rightarrow n+\Delta^{+})=\tfrac{1}{2}\sigma_{11}+\tfrac{1}{4}\sigma_{10}, \quad (11)$$

$$\sigma(p+p\rightarrow p+N^{*+})=0, \quad (12)$$

$$\sigma(n+p\rightarrow p+N^{*0})=\tfrac{3}{4}\sigma_{01}, \quad (13)$$

$$\sigma(n+p\rightarrow n+N^{*+})=\tfrac{3}{4}\sigma_{01}. \quad (14)$$

In the above, $\sigma_{if}(\sqrt{s})$ is defined as

$$\sigma_{if}(\sqrt{s})=\frac{\pi(\hbar c)^2}{2p^2}\,\alpha\left(\frac{p_r}{p_0}\right)^{\beta}\frac{m_0^2\Gamma^2(q/q_0)^3}{(s^*-m_0^2)^2+m_0^2\Gamma^2}, \quad (15)$$

where the parameters α, β, m_0, and Γ are listed in Table I. Other quantities in the parametrization are defined as in Ref. [15]. The cross section for the production of a $N^*(1535)$ resonance is estimated from the empirical η production cross section according to [18]

$$\sigma(NN\rightarrow NN^*(1535))\approx 2\sigma(NN\rightarrow NN\eta), \quad (16)$$

$$\sigma(pn\rightarrow pn\eta)\approx 3\sigma(pp\rightarrow pp\eta)=3\frac{0.102(\sqrt{s}-2.424)}{0.058+(\sqrt{s}-2.424)^2}\ (\text{mb}). \quad (17)$$

Cross sections for double resonance production in processes shown in Eq. (2) are estimated by subtracting from the measured inclusive 2π production cross section in the nucleon-nucleon collision [14] the contribution from $NN\rightarrow NN\rho$ and the 2π decay of the $N^*(1440)$ resonance in the $NN\rightarrow NN^*(1440)$ reaction. For example, we have for a pp collision,

$$\sigma\left(pp\rightarrow\sum_{I_\Delta I_\Delta}\Delta\Delta+\sum_{I_\Delta I_{N^*}}\Delta N^*(1440)\right)\equiv 4\sigma(pp\rightarrow pp\pi^+\pi^-)-2\sigma(pp\rightarrow pp\rho^0)-0.4\sigma(pp\rightarrow NN^*(1440)). \quad (18)$$

We show in Fig. 1 the experimental pp inelastic cross section (solid line) together with its decomposition into contributions from the production of various resonances. It is seen that for $\sqrt{s}\geq 3.0$ GeV the contribution from double resonance production, shown by the dotted line, is about one-third of the total inelastic cross section. We have assumed that the double resonance production cross sections are the same for all channels allowed by charge conservation. This approximation is strongly supported by recent theoretical studies based on the one-boson-exchange model [19].

The cross sections for ρ and ω production in reactions shown in Eq. (3) are taken directly from the experimental data [14]. As an example, we show in Fig. 2 the experimental cross sections for the reactions $pp\rightarrow pp\omega$ and $pp\rightarrow pp\rho^0$. The cross section for quasi-3π production $NN\rightarrow\Delta\Delta\pi$ is taken as the difference between the measured inclusive 3π and ω production cross sections. For a pp collision, we have

$$\sigma\left(pp\rightarrow\sum_{I_\Delta I_\pi}\Delta\Delta\pi\right)\equiv 3[\sigma(pp\rightarrow pp\pi^+\pi^-\pi^0)+\sigma(pp\rightarrow pn\pi^+\pi^+\pi^-)]-\sigma(pp\rightarrow pp\omega). \quad (19)$$

It is seen from Fig. 1 that quasi-3π production dominates the inelastic cross section in the energy region $\sqrt{s}\geq 3.5$ GeV which corresponds to the c.m. energies of colliding nucleon pairs in the early stage of heavy-ion collisions at AGS energies. We then attribute the difference between the experimental total nucleon-nucleon inelastic cross section and the sum of cross sections from reactions shown in Eqs. (1)–(3) as well as the kaon production cross sections from reactions shown later in Eq. (68) to the quasi-4π production process $NN\rightarrow\Delta\Delta\rho$ (thin solid line in Fig. 1). In this way, the total inelasticity of the nucleon-nucleon collision is properly treated as only a limited, though large, number of reactions have been incorporated. The errors introduced by this approximation for the quasi-4π production cross section is small. From Fig. 1, it is seen that the maximum cross section for the process $NN\rightarrow\Delta\Delta\rho$ at $(\sqrt{s})_{NN}=4.9$ GeV, corresponding to the c.m. energy of colliding nucleon pairs at a beam momentum of 11.6 GeV/c, is about 3.0 mb, which, however, has to be compared with the 13, 9, and 5 mb for the final states $\Delta\Delta\pi$, $\Delta\Delta+\Delta N^*$, and $N\Delta+NN^*$, respectively. Cross sections for reactions shown in Eqs. (5)–(7) are taken to be the same as in the nucleon-nucleon collision having the same center-of-mass energy and total charge.

Using the rejection method, the masses of Δ, $N^*(1440)$, $N^*(1535)$, and ρ are distributed according to the modified single or joint Breit-Wigner distributions with momentum-dependent widths. For single-resonance production, the cross section can be expressed in terms of the transition matrix element $\mathscr{M}_{NN'\rightarrow N''r}$:

$$\sigma(NN'\rightarrow N''r)=\frac{m_{r0}^2m_N^3}{\pi s p_i}\int_{m_N+m_\pi}^{\sqrt{s}-m_N}\frac{dm_r}{2\pi}P_1(m_r)\times\int\frac{d\Omega}{4\pi}\sum_{s_is_f}|\mathscr{M}_{NN'\rightarrow N''r}|^2, \quad (20)$$

where $P_1(m_r)$ is the modified Breit-Wigner function

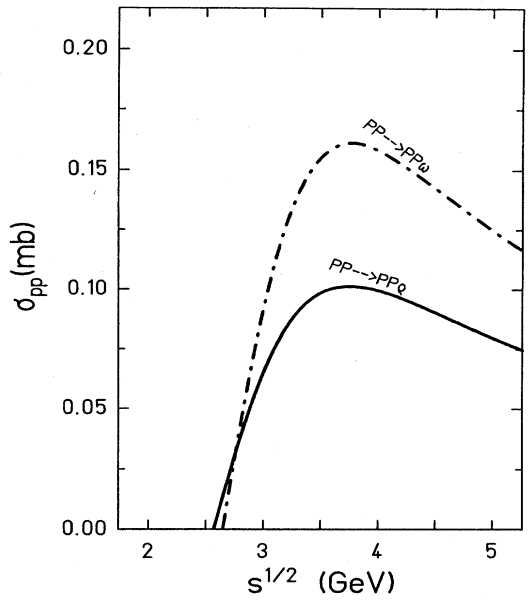

FIG. 2. $pp \to pp\omega$ and $pp \to pp\rho^0$ cross sections as functions of center-of-mass energy.

$$P_1(m_r) = \frac{p_f m_r \Gamma(m_r)}{(m_r^2 - m_{r0}^2)^2 + m_{r0}^2 \Gamma_r^2(m_r)} . \tag{21}$$

In the above, p_i and p_f are the nucleon momenta in the center-of-mass frame of NN' and $N''r$, respectively. The centroid and width of the resonance are denoted by m_{r0} and $\Gamma(m_r)$, respectively. As discussed in detail in Refs. [17,20], to obtain an accurate resonance mass distribution requires knowledge about the mass dependence of the matrix element. For simplicity, we assume that the matrix element is independent of the mass, and the mass distribution of the resonance is then given by $P_1(m_r)$. The momentum factor p_f in $P_1(m_r)$ plays an important role in collisions at energies near the threshold for resonance production as it suppresses the production of resonances with masses near the maximum mass $m_{\max} = \sqrt{s} - m_n$.

For double resonance production $NN' \to r_1 r_2$, one has

$$\sigma(NN' \to r_1 r_2) = \frac{4 m_n^2 m_{r10}^2 m_{r20}^2}{\pi s p_i (1 + \delta_{r_1 r_2})} \times \int\int \frac{dm_{r1} dm_{r2}}{4\pi^2} P_2(m_{r1}, m_{r2}) \times \int \frac{d\Omega}{4\pi} \sum_{s_i s_f} |\mathscr{M}_{NN' \to r_1 r_2}|^2 , \tag{22}$$

where $P_2(m_{r1}, m_{r2})$ is the joint Breit-Wigner function,

$$P_2(m_{r1}, m_{r2}) = \frac{p_f m_{r1} \Gamma_1}{[(m_{r1}^2 - m_{r10}^2)^2 + m_{r10}^2 \Gamma_1^2]} \times \frac{m_{r2} \cdot \Gamma_2}{[(m_{r2}^2 - m_{r20}^2)^2 + m_{r20}^2 \Gamma_2^2]} , \tag{23}$$

with the conditions

$$m_n + m_\pi \le m_{r1} \le \sqrt{s} - m_{r2} ,$$
$$m_n + m_\pi \le m_{r2} \le \sqrt{s} - m_n - m_\pi . \tag{24}$$

In Eq. (23), p_f is the momentum of the resonances in their center-of-mass frame. Unlike other models for heavy-ion collisions at AGS energies, resonances in our model can be produced with a large range of masses.

For reactions producing a ρ resonance, one has the similar expression for the production cross section. The ρ mass distribution is

$$P(m_\rho) = \frac{\Gamma^2(m_\rho)}{(m_\rho - 0.77)^2 + 0.25\Gamma^2(m_\rho)} . \tag{25}$$

Moreover, in calculating the masses, decay probabilities, and formation cross sections of baryon resonances, the following momentum-dependent widths are used:

$$\Gamma(\Delta(1232)) = 0.47 q^3/(m_\pi^2 + 0.6 q^2) \ \text{(GeV)}, \tag{26}$$

$$\Gamma(N^*(1440)) = 0.20 (q/q_0)^3 \ \text{(GeV)}, \tag{27}$$

$$\Gamma(N^*(1535)) = 0.15 (q/q_0) \ \text{(GeV)}, \tag{28}$$

where q_0 is the nucleon momentum in the rest frame of the resonance with its mass at the centroid. However, constant widths of 0.151 and 0.0084 GeV are used for ρ and ω, respectively.

The reverse reactions should be treated on the same footing. However, in the present version of the model, we have limited ourselves to only two-body collisions as indicated by the arrows in Eqs. (1)–(7). In view of the high baryon density reached in heavy-ion collisions at AGS energies, many-body interactions should become increasingly important as the compression gradually increases during the collision. Both the physics and techniques of treating many-body interactions are currently of great intreat but unfortunately without clear solution. We therefore postpone the inclusion of three-body and possibly many-body collisions to a later version of the model. Cross sections for the two-body reverse reactions are calculated by the detailed balance relation taking into account the finite widths of the resonances. For the absorption of a single resonance $N''r \to NN'$ we have the cross section

$$\sigma(N''r \to NN') = \frac{m_r m_N^3 p_i}{2 g_r \pi s p_f (1 + \delta_{NN'})} \times \int \frac{d\Omega}{4\pi} \sum_{s_i s_f} |\mathscr{M}_{N''r \to NN'}|^2 , \tag{29}$$

where $g_r = 4(2)$ is the spin degeneracy of the resonance $r = \Delta(N^*)$. The factor $(1 + \delta_{NN'})$ takes into account the case of having two identical nucleons in the final state. Using $|\mathscr{M}_{N''r \to NN'}|^2 = |\mathscr{M}_{NN' \to N''r}|^2$, Eqs. (20) and (29) lead to the following detailed balance relation [17]:

$$\sigma(N''r\to NN')=\frac{m_r}{2g_r m_{r0}^2}\frac{1}{(1+\delta_{NN'})}\frac{p_i^2}{p_f}\sigma(NN'\to N''r)\times\left(\int_{m_\pi+m_N}^{\sqrt{s}-m_N}\frac{dm_r'}{2\pi}P_1(m_r')\right)^{-1}. \quad (30)$$

Similarly, for the absorption of two resonances $r_1r_2\to NN'$ we have

$$\sigma(r_1r_2\to NN')=\frac{m_{r1}m_{r2}m_N^2 p_i}{g_{r1}g_{r2}\pi s(1+\delta_{NN'})p_f}\times\int\frac{d\Omega}{4\pi}\sum_{s_i s_f}|\mathscr{M}_{r_1r_2\to NN'}|^2. \quad (31)$$

The detailed balance relation in this case then reads as

$$\sigma(r_1r_2\to NN')=\frac{m_{r1}m_{r2}}{4g_{r_1}g_{r_2}m_{r10}^2m_{r20}^2}\frac{1+\delta_{r_1r_2}}{1+\delta_{NN'}}\frac{p_i^2}{p_f}\times\sigma(NN'\to r_1r_2)\times\left(\int\frac{dm_{r1}'}{2\pi}\frac{dm_{r2}'}{2\pi}P_2(m_{r1}',m_{r2}')\right)^{-1}. \quad (32)$$

Limits of the mass integration are given by Eq. (24). In the case, $P_1(m_r)=\pi p_f\delta(m_r-m_{r0})/(2m_{r0})$ and $\sqrt{s}\to\infty$, the above relations reduce to the standard detailed balance relations for the production and absorption of resonances with fixed masses

$$\sigma(N''r\to NN')=\frac{2}{g_r}\frac{1}{1+\delta_{NN'}}\frac{p_i^2}{p_f^2}\sigma(NN'\to N''r), \quad (33)$$

$$\sigma(r_1r_2\to NN')=\frac{4}{g_{r1}g_{r2}}\frac{1+\delta_{r_1r_2}}{1+\delta_{NN'}}\frac{p_i^2}{p_f^2}\sigma(NN'\to r_1r_2). \quad (34)$$

At AGS energies, resonances with large widths can be produced, especially in the early stage of the collisions; it is then necessary to use the detailed balance relations of Eqs. (30) and (32) to treat their annihilation.

B. Baryon-meson interactions

One can also separate meson-baryon interactions into the elastic and inelastic parts. For the elastic interaction, we treat them via the formation of baryon resonances

$$\pi N\leftrightarrow\Delta,N^*(1440),N^*(1535), \quad (35)$$

$$\eta N\leftrightarrow N^*(1535), \quad (36)$$

as well as direct reactions

$$\pi+N(\Delta,N^*)\to\pi+N(\Delta,N^*), \quad (37)$$

$$\rho+N(\Delta,N^*)\to\rho+N(\Delta,N^*), \quad (38)$$

$$K^++N(\Delta,N^*)\to K^++N(\Delta,N^*). \quad (39)$$

The standard Breit-Wigner form [21] of resonance formation in meson-nucleon interactions can be rewritten as

$$\sigma(M+N)=\sigma_{\max}\left(\frac{q_0}{q}\right)^2\frac{\frac{1}{4}\Gamma^2(m_r)}{(m_r-m_{r0})^2+\frac{1}{4}\Gamma^2(m_r)}, \quad (40)$$

where q_0 is the meson momentum at the centroid m_{r0} of the resonance mass distribution. The mass m_r of the produced baryon resonance is uniquely determined by reaction kinematics. The maximum cross sections are given by

$$\sigma_{\max}(\pi^++p\to\Delta^{++})=\sigma_{\max}(\pi^-+n\to\Delta^-)=190\ \text{mb}, \quad (41)$$

$$\sigma_{\max}(\pi^0+p\to\Delta^+)=\sigma_{\max}(\pi^0+n\to\Delta^0)=50\ \text{mb}, \quad (42)$$

$$\sigma_{\max}(\pi^-+p\to\Delta^0)=\sigma_{\max}(\pi^++n\to\Delta^+)=30\ \text{mb}, \quad (43)$$

$$\sigma_{\max}(\pi^-+p\to\mathrm{N}^{*0}(1440))=\sigma_{\max}(\pi^0+n\to\mathrm{N}^{*0}(1440))=6\ \text{mb}, \quad (44)$$

$$\sigma_{\max}(\pi^++n\to\mathrm{N}^{*+}(1440))=\sigma_{\max}(\pi^0+p\to\mathrm{N}^{*+}(1440))=12\ \text{mb}, \quad (45)$$

$$\sigma_{\max}(\pi^-+p\to\mathrm{N}^{*0}(1535))=\sigma_{\max}(\pi^0+n\to\mathrm{N}^{*0}(1535))=8\ \text{mb}, \quad (46)$$

$$\sigma_{\max}(\pi^++n\to\mathrm{N}^{*+}(1535))=\sigma_{\max}(\pi^0+p\to\mathrm{N}^{*+}(1535))=16\ \text{mb}, \quad (47)$$

$$\sigma_{\max}(\eta+p\to\mathrm{N}^{*+}(1535))=\sigma_{\max}(\eta+n\to\mathrm{N}^{*0}(1535))=74\ \text{mb}. \quad (48)$$

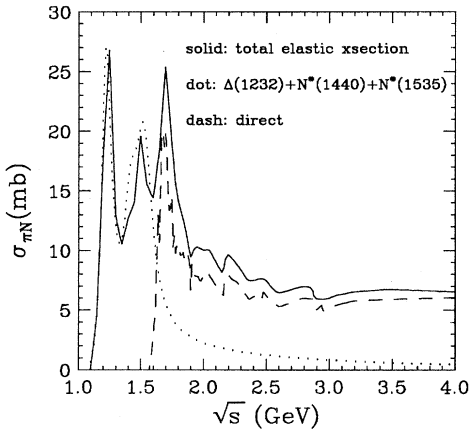

FIG. 3. The $\pi^- + p$ elastic cross section as a function of center-of-mass energy. The solid line is the experimental data and the dotted line is the contribution from the formation of $\Delta, N^*(1440)$, and $N^*(1535)$ resonances. The dashed line is the difference between the solid and dotted lines and is attributed to direct $\pi + N$ scattering.

In evaluating $\sigma_{\max}$, we have taken into account properly the decay branching ratios of the $N^*(1440)$ and $N^*(1535)$ resonances.

The formation of the three baryon resonances in the reactions shown in Eq. (35) accounts almost entirely the $\pi + N$ elastic cross sections at low energies. This is demonstrated in Fig. 3 and Fig. 4 where the experimental cross sections for the elastic scattering of $\pi^- + p$ and $\pi^+ + p$ are compared with the sum of the three baryon resonance formation cross sections. It is also seen from the figures that the formation of the Δ resonance alone is not enough to describe even the low energy part of $\pi + N$ scattering. At higher energies, the elastic cross section is mainly due to the formation of higher resonances which are not included in the present version of the model. We therefore attribute the difference between the experimental elastic cross section and the contribution from the three lowest baryon resonances to the direct process $\pi + N \to \pi + N$. The contribution from direct $\pi + N$ scattering is shown by the dotted lines in Fig. 3 and Fig. 4.

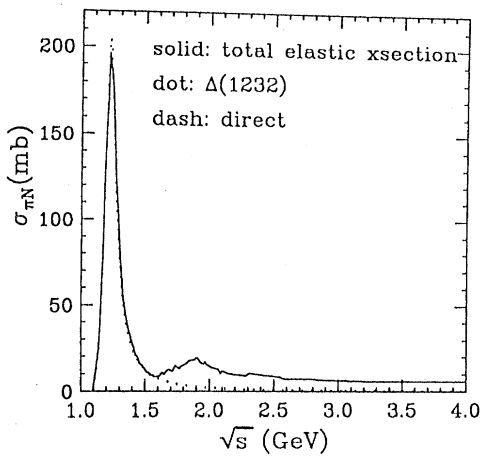

FIG. 4. $\pi^+ + p$ elastic cross section as a function of center-of-mass energy. The solid line is the experimental data and the dotted line is the contribution from the formation of the Δ resonance. The dashed line is the difference between the solid and dotted lines and is attributed to direct $\pi + N$ scattering.

TABLE II. Higher N^* resonances.

R	J^p	Mass	Width	$N\pi$	$\Delta\pi$	$N\rho$
D_{13}	$\frac{3}{2}^-$	1.520	0.125	0.550	0.250	0.200
S_{11}	$\frac{1}{2}^-$	1.650	0.150	0.600	0.050	0.180
D_{15}	$\frac{5}{2}^-$	1.675	0.155	0.380	0.580	0.030
F_{15}	$\frac{5}{2}^+$	1.680	0.125	0.600	0.125	0.125
D_{13}	$\frac{3}{2}^-$	1.700	0.100	0.100	0.380	0.100
P_{11}	$\frac{1}{2}^+$	1.710	0.110	0.150	0.100	0.200
P_{13}	$\frac{3}{2}^+$	1.720	0.200	0.150	0.100	0.530
F_{17}	$\frac{7}{2}^+$	1.990	0.290	0.050	0.060	0.340

The experimentally unknown cross sections, such as those for $\pi^0 + N$, $\pi + \Delta(N^*)$, and $\rho + N(\Delta, N^*)$ reactions, are calculated by using a resonance model that includes heavier baryon resonances with masses up to about 2.0 GeV. Neglecting interferences between resonances, one has

$$\sigma(M+B) = 1.3\frac{\pi}{k^2}\sum_R \frac{(2J_R+1)}{(2S_M+1)(2S_B+1)} \times \frac{\Gamma_R^2(M+B)}{(\sqrt{s}-m_R)^2 + 0.25\Gamma_R^2(\text{total})}. \quad (49)$$

The prefactor 1.3 is introduced so that the high energy part of $\pi^+ + p$ data can be fitted and is mainly due to the neglect of interferences. The summation is over all baryon resonances with masses up to 2 GeV. The total width $\Gamma_R(\text{total})$ and partial widths $\Gamma_R(M+B)$ of heavier N^* and Δ resonances used in the summation are listed in Table II and Table III, respectively. For illustrations, we show in Fig. 5 and Fig. 6 the calculated $\pi^0 + p(n)$ and $\pi^+ + \Delta^-(\Delta^0)$ elastic cross sections. For the $K^+ + N(\Delta, N^*)$ scattering a constant cross section of 10 mb is used according to the available data.

TABLE III. Higher Δ resonances.

R	J^p	Mass	Width	$N\pi$	$\Delta\pi$	$N\rho$
P_{33}	$\frac{3}{2}^+$	1.600	0.250	0.350	0.450	0.050
S_{31}	$\frac{1}{2}^-$	1.620	0.160	0.300	0.600	0.070
D_{33}	$\frac{3}{2}^-$	1.700	0.280	0.150	0.698	0.150
S_{31}	$\frac{1}{2}^-$	1.900	0.150	0.100	0.050	0.450
F_{35}	$\frac{5}{2}^+$	1.905	0.300	0.100	0.250	0.450
P_{31}	$\frac{1}{2}^+$	1.910	0.220	0.220	0.089	0.060
P_{33}	$\frac{3}{2}^+$	1.920	0.250	0.200	0.190	0.080
D_{35}	$\frac{5}{2}^-$	1.930	0.250	0.090	0.200	0.120
F_{37}	$\frac{7}{2}^+$	1.950	0.240	0.400	0.130	0.080

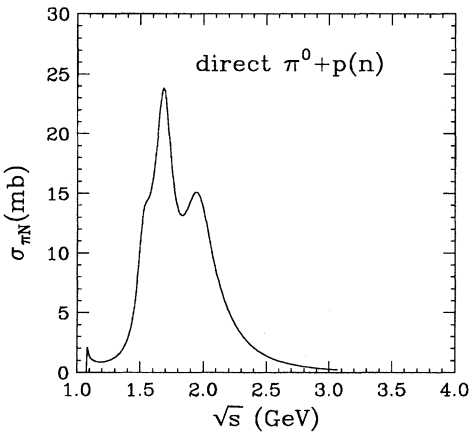

FIG. 5. The $\pi^0+p(n)$ elastic cross section as a function of center-of-mass energy calculated from the resonance model.

The decay of resonances, such as $\Delta(N^*(1440), N^*(1535))\rightarrow\pi+N$, $N^*(1440)\rightarrow 2\pi+N$, $N^*(1535)\rightarrow\eta+N$, $\rho\rightarrow 2\pi$, and $\omega\rightarrow 3\pi$, during each time step of length dt are treated by the Monte Carlo method. The decay probability of a resonance is calculated via

$$P_{\text{decay}}=1-\exp[-dt\Gamma(m_r)/(\gamma\hbar)], \tag{50}$$

where $\gamma=E/m_r$ is the Lorentz factor associated with the moving resonance. For the decay of $N^*(1440)$ and $N^*(1535)$ resonances the actual final state is chosen according to the corresponding branching ratios. Namely, $B(N^*(1440)\rightarrow\pi+N)=0.6$, $B(N^*(1440)\rightarrow 2\pi+N)=0.4$ for $m(N^*(1440))\geq 2m_n+m_\pi$; otherwise $B(N^*(1440)\rightarrow\pi+N)=1$. For the $N^*(1535)$ resonance we use $B(N^*(1535)\rightarrow\pi+N)\approx B(N^*(1535)\rightarrow\eta+N)=0.5$. Finally, Λ and Σ are allowed to decay into a nucleon and a pion only at the very end of the reaction. It is worthy to mention that the Bose-Einstein enhancement factor $(1+f_\pi)$ for a pion in the final state has not been included in meson +nucleon collisions and decays of resonances. This is certainly another aspect to be improved in a later version of the model in view of the high pion densities reached in heavy-ion collisions at AGS energies.

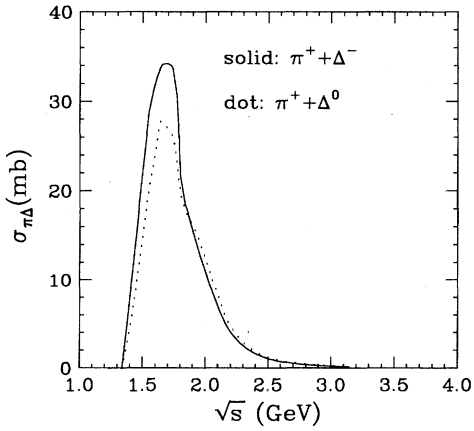

FIG. 6. The $\pi^+ + \Delta^-(\Delta^0)$ elastic cross section as a function of center-of-mass energy calculated from the resonance model.

The $\pi+N$ inelastic collision starts at $(\sqrt{s})_{\pi N}\approx 1.2$ GeV due to the $\pi\pi N$ final state. As the energy increases the number of final state quickly increases to the order of 200. Most inelastic reactions lead to pion and kaon production. The final states can also consist of baryon and meson resonances. To treat the inelastic reactions in a numerically tractable way, we model them through the production of Δ, ρ, and ω resonances, i.e.,

$$\pi+N\leftrightarrow\Delta+\pi, \tag{51}$$

$$\pi+N\leftrightarrow\Delta+\rho, \tag{52}$$

$$\pi+N\leftrightarrow\Delta+\omega, \tag{53}$$

and those producing kaons shown later in Eq. (75). We have thus included only final states with at most four quasipions. Again, the above decomposition of the cross sections involves some uncertainties and approximations. However, as we will discuss later our final results are not sensitive to them due to the large number of final-state interactions.

For two- and three-pion production in $\pi+N$ collisions, we assume that they are mainly through the production of $\Delta\pi$ and $\Delta\rho$, respectively. For example, for the $\Delta\pi$ final state in the $\pi^+ + p$ interaction, we use

$$\begin{aligned}\sigma\left(\pi^+p\rightarrow\sum_{I_\Delta I_\pi}\Delta\pi\right)\equiv&\,\sigma(\pi^+p\rightarrow p\pi^+\pi^0)\\&+\sigma(\pi^+p\rightarrow n\pi^+\pi^+)\\&+\sigma(\pi^+p\rightarrow p\rho^+)\\&+2\sigma(\pi^+p\rightarrow\Delta^{++}\pi^0),\end{aligned} \tag{54}$$

and for the $\Delta\rho$ final state, we use

$$\begin{aligned}\sigma\left(\pi^+p\rightarrow\sum_{I_\Delta I_\rho}\Delta\rho\right)\equiv&\,3\sigma(\pi^+p\rightarrow p\pi^+\pi^+\pi^-)\\&+3\sigma(\pi^+p\rightarrow p\pi^+\rho^0)\\&+2\sigma(\pi^+p\rightarrow\Delta^{++}\rho^0)\\&+\sigma(\pi^+p\rightarrow p\omega).\end{aligned} \tag{55}$$

The difference between the experimental total $\pi+N$ inelastic cross section and the cross sections for producing $\Delta\pi$, $\Delta\rho$, and kaons are then attributed to the production of $\Delta\omega$, i.e.,

$$\begin{aligned}\sigma(\pi^+p\rightarrow\Delta^+\omega)\equiv&\,\sigma^{\text{inel}}_{\text{expt}}(\pi^+p)-\sigma\left(\pi^+p\rightarrow\sum_{I_\Delta I_\pi}\Delta\pi\right)\\&-\sigma\left(\pi^+p\rightarrow\sum_{I_\Delta I_\rho}\Delta\rho\right)\\&-\sigma(\pi^+p\rightarrow K^+X).\end{aligned} \tag{56}$$

As an example, the decomposition of the inelastic $\pi^+ + p$ cross section is shown in Fig. 7. It is seen that the cross sections for having two, three, and four quasipions are com-

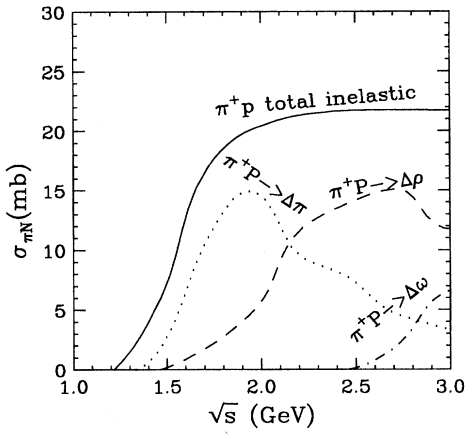

FIG. 7. The $\pi^+ + p$ inelastic cross section as a function of the center-of-mass energy $\sqrt{s}$.

parable at $\sqrt{s} \approx 2.5$ GeV, but at higher energies the 4π channel dominates. As we shall see later, the distribution of meson+baryon center-of-mass energies peaks at about $\sqrt{s} \approx 1.5$ GeV in the reaction of Au+Au at $P_{\text{beam}}/A = 11.6$ GeV/c and falls off very quickly towards $\sqrt{s} \approx 2.5$ GeV. It thus makes us feel rather confident that the errors introduced in the quasi-4π channel in our previous decomposition is very small. The two-body reverse reactions of the $\pi + N$ inelastic collisions are similarly treated as for the two-body reverse reactions of the inelastic baryon-baryon collisions.

C. Meson-meson interactions

We model pion-pion elastic collisions through the formation of a ρ meson, i.e., $\pi + \pi \leftrightarrow \rho$, and the direct process $\pi + \pi \rightarrow \pi + \pi$. The latter takes into account the case when the quantum numbers of colliding pions forbid the formation of a P_{11} meson ρ.

In terms of the channel isospin cross sections σ^I with $I=0$, 1, and 2, one finds using the Glebsch-Gordan coefficients the following isospin decomposition of $\pi\pi$ scattering cross sections:

$$\sigma(\pi^+\pi^+) = \sigma(\pi^-\pi^-) = \sigma^2, \tag{57}$$

$$\sigma(\pi^+\pi^0) = \sigma(\pi^-\pi^0) = \tfrac{1}{2}\sigma^2 + \tfrac{1}{2}\sigma^1, \tag{58}$$

$$\sigma(\pi^+\pi^-) = \tfrac{1}{6}\sigma^2 + \tfrac{1}{2}\sigma^1 + \tfrac{1}{3}\sigma^0, \tag{59}$$

$$\sigma(\pi^0\pi^0) = \tfrac{1}{3}\sigma^0 + \tfrac{2}{3}\sigma^2, \tag{60}$$

$$\sigma(\pi^+\pi^- \leftrightarrow \pi^0\pi^0) = -\tfrac{1}{3}\sigma^0 + \tfrac{1}{3}\sigma^2. \tag{61}$$

Because of the symmetrization of two-pion states, only even partial waves are allowed for σ^0 and σ^2 and odd partial waves for σ^1. Low energy $\pi\pi$ scatterings are therefore described by the three partial-wave cross sections σ_0^0, σ_0^2, and σ_1^1. The formation of a ρ resonance has thus the probability

$$P_\rho(\pi\pi) = \frac{1}{2}\,\frac{\sigma_1^1}{\sigma(\pi\pi)}, \tag{62}$$

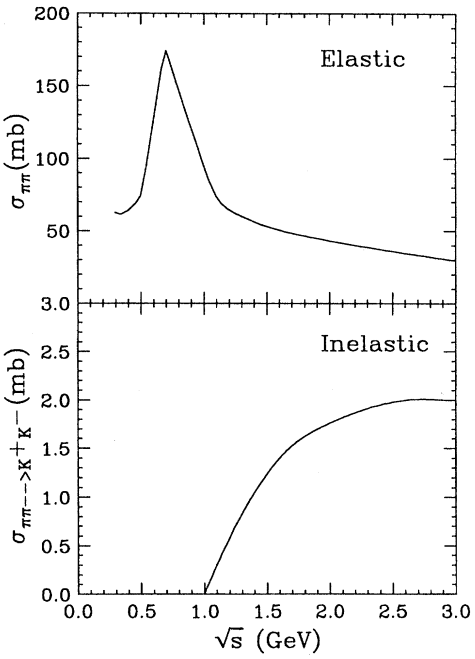

FIG. 8. The isospin-averaged $\pi\pi$ elastic (upper window) and inelastic (lower window) cross sections as functions of center-of-mass energy $\sqrt{s}$.

while the direct $\pi\pi \rightarrow \pi\pi$ reaction has the probability of $1 - P_\rho(\pi\pi)$.

The partial wave cross sections σ_L^I are related to the phase shift δ_L^I via

$$\sigma_L^I = \frac{8\pi}{q^2}(2L+1)\sin^2\delta_L^I, \tag{63}$$

where q is the momentum of the pion in the center of mass of the two pions. For δ_L^I we use the parametrization of Ref. [22]:

$$\delta_0^0 = \tan^{-1}\left(\frac{1.03q}{5.8m_\pi - \sqrt{s}}\right), \tag{64}$$

$$\delta_1^1 = \tan^{-1}\left(\frac{\Gamma_\rho/2}{0.77 - \sqrt{s}}\right), \tag{65}$$

$$\delta_0^2 = -0.12q/m_\pi, \tag{66}$$

where $\Gamma_\rho = 0.095q[(q/m_\pi)/(1+(q/0.77)^2)]^2$. The isospin-averaged cross section for $\pi\pi$ scattering,

$$\bar{\sigma}(\pi\pi) = \tfrac{1}{9}\sigma_0^0 + \tfrac{1}{3}\sigma_1^1 + \tfrac{5}{9}\sigma_0^2, \tag{67}$$

is shown in the upper window of Fig. 8 as a function of the center-of-mass energy $\sqrt{s}$. Since the densities of ρ and ω are rather small at AGS energies, we have neglected in the present version of the model the elastic scattering of $\pi+\rho, \pi+\omega$, and $\rho+\omega$.

The inelastic collisions among mesons are modeled through the reaction $MM \rightarrow K\bar{K}$. The cross section for this

reaction is highly uncertain; here we use the cross section calculated from the K^*-exchange model of Ref. [23]. The lower window of Fig. 8 shows the isospin-averaged cross section for the reaction $\pi\pi \to K\bar{K}$. Calculated cross sections in Ref. [23] for the reactions $\rho\rho \to K\bar{K}$ and $\pi\rho \to K\bar{K}$ have values about 0.3 mb, except at energies very close to the threshold, which we shall use in our model. Furthermore, we assume that for the reactions $\pi\omega \to K\bar{K}$ and $\rho\omega \to K\bar{K}$, the cross sections have similar values.

D. K^+ production in baryon-baryon and baryon-meson interactions

We are at present mainly interested in K^+ production. The following kaon production channels in baryon-baryon collisions are included:

$$NN \to N\Lambda(\Sigma)K, \quad \Delta\Lambda(\Sigma)K, \tag{68}$$

$$NR \to N\Lambda(\Sigma)K, \quad \Delta\Lambda(\Sigma)K, \tag{69}$$

$$RR \to N\Lambda(\Sigma)K, \quad \Delta\Lambda(\Sigma)K, \tag{70}$$

where R denotes a Δ, $N^*(1440)$, or $N^*(1535)$. We use the approximation that the kaon production cross sections in reactions induced by resonances are the same as in nucleon-nucleon collisions at the same center-of-mass energy which are mainly taken from the data compilation of Refs. [14,24]. Since the experimental data on kaon production are very limited, we use only the isospin-averaged cross sections. Based on the one-pion exchange model these cross sections can be expressed in terms of the experimentally known ones [25]:

$$\bar{\sigma}\,(NN \to N\Lambda K^+) \approx \bar{\sigma}\,(NN \to \Delta\Lambda K^+) \approx \frac{3}{2}\,\sigma(pp \to p\Lambda K^+), \tag{71}$$

$$\bar{\sigma}\,(NN \to N\Sigma K^+) \approx \bar{\sigma}\,(NN \to \Delta\Sigma K^+) \approx \frac{3}{2}\,[\sigma(pp \to p\Sigma^0 K^+) + \sigma(pp \to p\Sigma^+ K^0)]. \tag{72}$$

The threshold energies are 2.56, 2.74, 2.63, and 2.77 GeV for the four final states $N\Lambda K$, $\Delta\Lambda K$, $N\Sigma K$, and $\Delta\Sigma K$, respectively. The actual final state of a given collision is determined using the Monte Carlo method according to the relative ratios among these cross sections.

The kaon momentum distribution from a baryon-baryon interaction was parametrized by Randrup and Ko according to a modified phase space [25], i.e.,

$$\frac{E}{p^2}\frac{d^3\sigma(\sqrt{s})}{dp\,d\Omega} = \sigma_{K^+}(\sqrt{s})\,\frac{E}{4\pi p^2}\,\frac{12}{p_{\max}}\left(1 - \frac{p}{p_{\max}}\right)\left(\frac{p}{p_{\max}}\right)^2, \tag{73}$$

where $p_{\max}$ is the maximum kaon momentum given by

$$p_{\max} = \frac{1}{2}\sqrt{[s - (m_B + m_Y + m_K)^2][s - (m_B + m_Y - m_K)^2]/s}. \tag{74}$$

The angular distribution is taken as isotropic in the center-of-mass frame of colliding baryons.

In meson-baryon interactions, kaons are produced through

$$\pi + N(\Delta, N^*) \to \Lambda(\Sigma) + K, \tag{75}$$

$$\rho + N(\Delta, N^*) \to \Lambda(\Sigma) + K, \tag{76}$$

$$\omega + N(\Delta, N^*) \to \Lambda(\Sigma) + K. \tag{77}$$

For pion-nucleon collisions, the isospin-averaged cross sections for kaon production can be expressed in terms of the available data [27]:

$$\bar{\sigma}\,(\pi N \to \Lambda K^+) \approx \frac{1}{4}\,\sigma(\pi^+ n \to \Lambda K^+), \tag{78}$$

$$\bar{\sigma}\,(\pi N \to \Sigma K^+) \approx \frac{1}{4}\,[\sigma(\pi^- p \to \Sigma^- K^+) + \sigma(\pi^- p \to \Sigma^0 K^0) + \sigma(\pi^+ p \to \Sigma^+ K^+)]. \tag{79}$$

Since there are no data available for kaon production in resonance induced reactions [e.g., $\rho(\omega)+N(\Delta,N^*)$ and $\pi+\Delta(N^*)$], they are taken for simplicity to be the same as in the $\pi+N$ collision at the same center-of-mass energy. This is probably a resonable, minimal assumption one can make. However, it is interesting to note that theoretical efforts have recently been made to calculate these unknown cross sections (e.g., [26]), and we plan to incorporate these results in future versions of the ART model.

The experimental information about the angular distribution of the outgoing kaon in a meson-baryon collision is rather sparse but shows a complicated structure [27]. Here, we use an isotropic distribution in the meson-baryon center-of-mass frame. A test using a forward-backward peaked angular distribution in the baryon-meson c.m. frame shows little change in the final kaon distribution in heavy-ion collisions as a result of kaon final-state interactions.

Finally, we would like to point out that in reactions $RN\rightarrow NYK$ and $RR\rightarrow NYK$, which are dominated by one-pion exchange, the pion can be on-shell. The latter contribution is equivalent to a two-step process, i.e., a resonance decaying into a physical pion and a nucleon, and the subsequent production of a kaon from the pion-baryon interaction. To avoid double counting, one can follow the approach of Ref. [28] by including only the reactions $RN\rightarrow NYK$ and $RR\rightarrow NYK$ but not the reaction $\pi B\rightarrow NYK$. This requires, however, a model for the reactions $RN\rightarrow NYK$ and $RR\rightarrow NYK$. In the present paper, we use instead the assumption that the cross sections for the reactions $RN\rightarrow NYK$ and $RR\rightarrow NYK$ due to off-shell pions are the same as in $NN\rightarrow NYK$ reaction at the same center-of-mass energy, which invloves only an off-shell pion. Then, we should include both the reactions $RN\rightarrow NYK$ and $RR\rightarrow NYK$ and the reactions $\pi B\rightarrow NYK$ in the transport model.

E. Hadron momentum distributions

In this section, we discuss the method we use to determine the final particle momenta in a hadron-hadron collision, which does not involve kaons. In principle, to determine the momentum of a particle in a multiparticle production process, one needs to know the interaction matrix element which is model dependent. For simplicity, we determine the momentum distribution of the produced particles according to the phase space. Besides imposing the energy-momentum conservation, we also make use of the systematics observed in multiparticle production processes. These systematics are often given by empirical formula that are fitted to the inclusive data.

An important feature of energetic hadron-hadron collisions is the "leading" particle behavior. In our model this is ensured by requiring the outgoing baryons to have the same or similar identities as the incident ones so that their longitudinal directions are retained when performing the momentum transformation from the baryon-baryon c.m. frame to the nucleus-nucleus c.m. frame. Moreover, baryons in the final state of an energetic hadron-hadron collision have a typical forward-backward peaked angular distribution and a soft transverse momentum distribution. For baryon-baryon collisions with $\sqrt{s}\leq 3.0$ GeV where single-resonance production

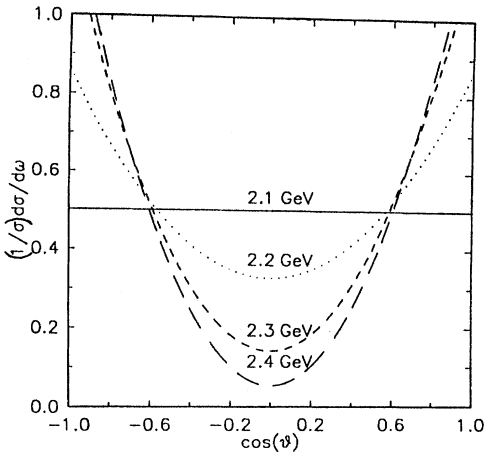

FIG. 9. The angular distribution of $NN\rightarrow N\Delta$ reaction at different center-of-mass energies.

dominates, we use the angular distribution obtained from fitting the $pp\rightarrow N\Delta$ data [16], i.e.,

$$\frac{1}{\sigma}\frac{d\sigma}{d\Omega}=b_1(s)+3b_3(s)\cos^2\theta, \tag{80}$$

where $b_1(s)=0.5$ and $b_3(s)=0$ for $\sqrt{s}\leq 2.14$ GeV, and

$$b_1(s)=29.03-23.75\sqrt{s}+4.87s, \tag{81}$$

$$b_3(s)=-30.33+25.53\sqrt{s}-5.30s, \tag{82}$$

for $2.14\leq\sqrt{s}\leq 2.4$ GeV, while for $2.4\leq\sqrt{s}\leq 3.0$ GeV, $b_1(s)=0.06$, $b_3(s)=0.4$. This distribution is shown in Fig. 9, and it is seen that the forward-backward peaked angular distribution becomes almost energy independent for $\sqrt{s}\geq 2.3$ GeV. This tendency is consistent with the systematics found in pp collisions at high energies where the inclusive proton spectra can be well described by [29]

$$\frac{d^2N}{d^3\vec{p}^*}=\frac{1.39}{\sqrt{s}}(1.+0.43x^*-0.84x^{*2})(e^{-3.78p_t^2}+0.47e^{-3.6p_t}), \tag{83}$$

with x^* being the scaled longitudinal momentum in the c.m. frame, i.e., $x^*=2p_z^*/\sqrt{s}$. The distribution has the properties of the naive scaling, p_t and p_z^* factorization, and the soft, energy-independent transverse momentum distribution.

Here we adopt the same functional form of momentum distribution as given by Eq. (83) for all baryons in collisions with $\sqrt{s}\geq 3.0$ GeV, but slightly adjust the parameters in the transverse momentum distribution so that we can reproduce the inclusive proton momentum distribution from pp collisions at $P_{\rm beam}=15$ GeV/c. Although both longitudinal and transverse momentum distributions are needed for three-body final states, only the transverse momentum distribution is required for two-body final states as the longitudinal momentum can be determined from the momentum conserva-

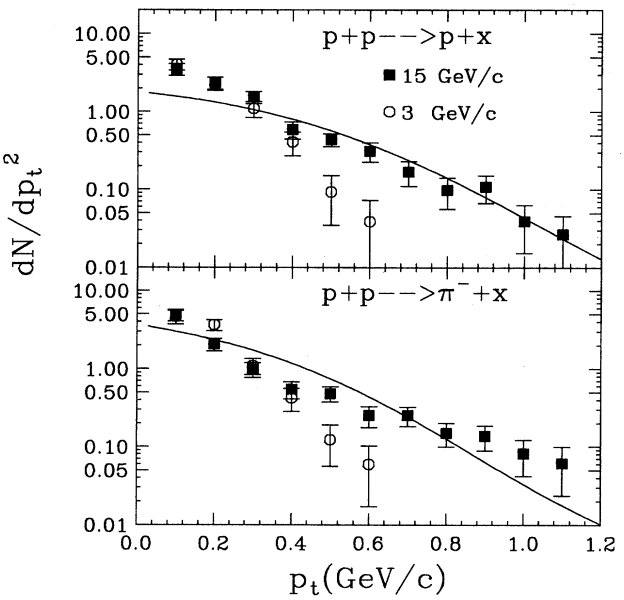

FIG. 10. Transverse momentum distributions for protons (upper window) and pions (lower window) from pp collisions at $p_{\text{beam}}=15$ GeV/c and 3 GeV/c. Solid lines are the scaling results valid at high energies as discussed in the text.

tion. The momentum distribution determined by the present model turns out to be very similar to Eq. (83), i.e.,

$$\frac{d^2N}{d^3\vec{p}^*} \propto (1.+0.5x^*-0.9x^{*2})(e^{-4p_t^2}+0.5e^{-10p_t}). \quad (84)$$

In the upper window of Fig. 10, the proton transverse momentum distribution from pp collisions at $p_{\text{beam}}=15$ GeV/c, which is used to determine the input momentum distribution in Eq. (84), is shown by the solid squares. The solid line is a plot of the proton transverse momentum distribution from Eq. (83). The quality of the fit is reasonably good although there is still some room at low transverse momenta for further improvement. The longitudinal momentum distribution has a very similar behavior. With the above transverse momentum distribution for baryons and employing the assumption that all resonances decay isotropically in their rest frames we obtain the transverse momentum distribution of π^- as shown in the lower window of Fig. 10. The π^- transverse momentum distribution is then seen to fit reasonably well the empirical formula

$$\frac{dN}{dp_t^2}(\pi^-) \propto (e^{-5.2p_t^2}+0.81e^{-4.3p_t}) \quad (85)$$

of Ranft *et al.* [29] for high energy pp collisions. For comparisons, we have also shown in Fig. 10 the generated proton and π^- transverse momentum distributions from pp collisions at $p_{\text{beam}}=3.0$ GeV/c. They, of course, do not agree with the scaling formula valid at high energies.

The above procedure makes us feel confident about our model for high energy heavy-ion collisions. We remark here, however, that there is no direct, transparent extrapolation from $p+p$, $p+A$, to AA collisions. The dynamics and the final momentum distributions of hadrons in heavy-ion collisions are rather sensitive to the modeling or prescription of individual hadron-hadron scattering, besides the elementary momentum distributions discussed above.

F. Nuclear equation of state and causality

The nuclear equation of state describes the response of the nuclear matter to changes in excitation energies and densities. Current knowledge on the nuclear equation of state is restricted to a narrow region around the ground state. Extending our knowledge about the nuclear equation of state to different densities and/or excitation energies has been a major goal of nuclear physics.

Mean-field effects have already been found to be important in heavy-ion collisions at medium energies. At higher energies such as at AGS, they have been ignored in ARC, for example. We believe that the mean-field potential is not negligible in heavy-ion collisions at AGS energies. Although the forward scattering amplitudes of hadron-hadron collisions in the high energy limit have been found approximately purely imaginary [30], the AGS energies may not be high enough for the real part of the scattering amplitude to completely vanish. Of course, the form and strength of the mean field in hot dense hadronic matter is uncertain and has been a subject of many discussions. Second, although in the early stage of the collision the kinetic energy is much higher than the potential energy, particles are gradually slowed down and the mean field is expected to play an increasingly important role as the collision proceeds. In particular, the repulsive mean field in the high density region tends to keep particles from coming close and therefore reduces the maximum energy and baryon densities reached in the collision should there be no mean field. Moreover, in the expansion phase of the collision mean-field effects become even stronger. It is therefore essential to study how the collision dynamics is affected by the nuclear mean field. Of course, the most challenging task is to identify the experimentally observable consequences of the nuclear mean field, and so the information about the nuclear equation of state can be obtained.

Without much reliable knowledge about the equation of state in hot dense medium, we use here the simple, Skyrme-type parametrization for the mean field which has been widely used in heavy-ion collisions at and below Bevalac energies,

$$U(\rho)=a\frac{\rho}{\rho_0}+b\left(\frac{\rho}{\rho_0}\right)^{\sigma}+V_{\text{Coulomb}}. \quad (86)$$

The corresponding energy per nucleon in nuclear matter at zero temperature is given by

$$\frac{E}{A}=\frac{a}{2}\left(\frac{\rho}{\rho_0}\right)+\frac{b}{1+\sigma}\left(\frac{\rho}{\rho_0}\right)^{\sigma}+\frac{3}{5}E_f\left(\frac{\rho}{\rho_0}\right)^{2/3}, \quad (87)$$

where $E_f=37.26$ MeV is the Fermi energy. The parameter a is negative, b is positive, and σ is larger than 1 reflecting the fact that the nucleon-nucleon interaction has a short-range repulsive part and a long-range attractive part. By fitting to

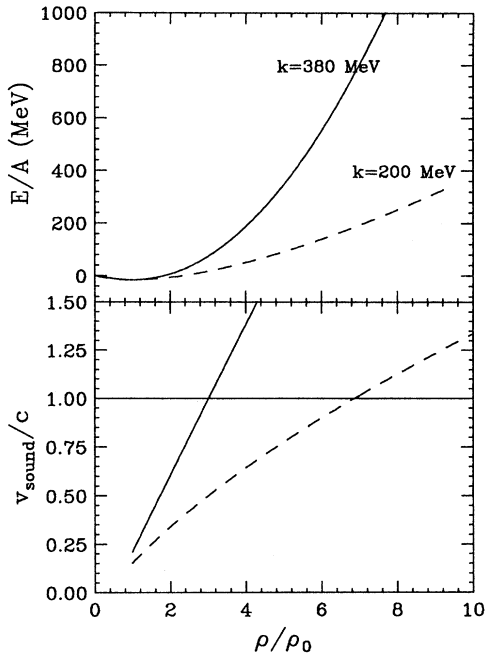

FIG. 11. The average energy per nucleon (upper window) and the adiabatic sound velocity (lower window) as functions of density in nuclear matter at zero temperature.

the ground-state properties of nuclear matter the three parameters are determined in terms of the compressibility coefficient K as

$$a=-29.81-46.90\frac{K+44.73}{K-166.32}\ (\mathrm{MeV}), \tag{88}$$

$$b=23.45\frac{K+255.78}{K-166.32}\ (\mathrm{MeV}), \tag{89}$$

$$\sigma=\frac{K+44.73}{211.05}. \tag{90}$$

The compressibility coefficient K can also be expressed in terms of a, b, and σ, i.e.,

$$K=9\rho(\partial P/\partial\rho)_s=9\left(\frac{p_f^2}{3m}+a+b\sigma\right). \tag{91}$$

An important constraint on the nuclear equation of state in hot dense medium is imposed by the causality [31,32]. For nuclear matter at zero temperature the adiabatic sound velocity is

$$V_s^2=\frac{1}{m}\left(\frac{\partial P}{\partial\rho}\right)_s=\frac{1}{m}\left[\frac{2}{3}E_f\left(\frac{\rho}{\rho_0}\right)^{2/3}+a\frac{\rho}{\rho_0}+b\sigma\left(\frac{\rho}{\rho_0}\right)^{\sigma}\right]. \tag{92}$$

The causal requirement $V_s^2\leq c^2$ limits the density range applicable for a given parameter set. In Fig. 11, we show the adiabatic sound velocity and the energy per nucleon as functions of density for the two equations of state corresponding to $K=377$ MeV ($\sigma=2$, stiff) and 201 MeV ($\sigma=7/6$, soft). It is seen that the stiff and soft equations of state violate the causality beyond densities $\rho\geq 3\rho_0$ and $\rho\geq 7\rho_0$, respectively. At finite temperatures the critical densities are reduced by less than one density unit [32]. In the following, we shall use the soft equation of state, and the stiff equation of station will only be mentioned for the purpose of discussions.

The mean-field potentials for baryon resonances are likely to be different from that of nucleons. Resonance potentials have been studied previously [33] and are still less uncertain [34] than the nucleon potential. For example, significant efforts have been devoted to understanding the effects of the Δ potential on the nuclear matter saturation properties [34–37]. The Δ optical potential has also been studied in charge-exchange reactions [38] and electron- and γ-induced reactions [39] as well as π-nucleus scattering [40,41]. All studies indicate that the shape of the Δ potential is very similar to the nucleon potential, probably a little deeper than the nucleon potential. The exact form of the Δ potential somehow depends on the momentum and density. Current theories give a large range of model parameters for the Δ potential, and they often have conflicting features. In view of the larger uncertainties associated with resonance potentials, we assume here that they are the same as the nucleon potential.

Since a large number of baryon resonances is produced in heavy-ion collisions at AGS energies, the reaction dynamics might be significantly affected by the resonance potentials. Relativistic heavy-ion collisions may therefore provide valuable information about the resonance potentials. However, this can only be possible if other details of the collision dynamics are well understood. The present work is thus also useful in this respect.

III. APPLICATION OF ART 1.0 TO HEAVY-ION COLLISIONS AT AGS ENERGIES

We first discuss the range of beam energies in which the model outlined above is applicable. In the energy range of $E_{\mathrm{beam}}/A\leq 3.0$ GeV/nucleon, our model, as many other nuclear transport models, is able to describe many aspects of heavy-ion collisions. These include the emission of light particles, the creation of pions, kaons, and etas as well as the transverse collective flow of various hadrons [42,43]. Since the particle production mechanism used in the model is exclusively based on the excitation and decay of several low-mass baryon and meson resonances, the model is expected to be inadequate once the energy is above about $E_{\mathrm{beam}}/A=15$ GeV. At higher energies, such as the SPS-CERN energies, heavier resonances and more importantly the formation and fragmentation of strings and ropes are expected to be the dominant mechanisms for particle production [2].

The model ART 1.0 is designed intentionally to be most applicable in heavy-ion collisions below the AGS energies. As in other hadronic models, our model is naturally limited only to interactions among hadrons. If there were a phase transition to the QGP at AGS, hadronic models, such as the present one, are still useful as their predictions provide the background against which new physical phenomena can be identified. In fact, one of the motivations for the present work is to study whether and how conditions for forming the quark-gluon plasma can be achieved in heavy-ion collisions at beam energies from 2 GeV/nucleon up to AGS energies.

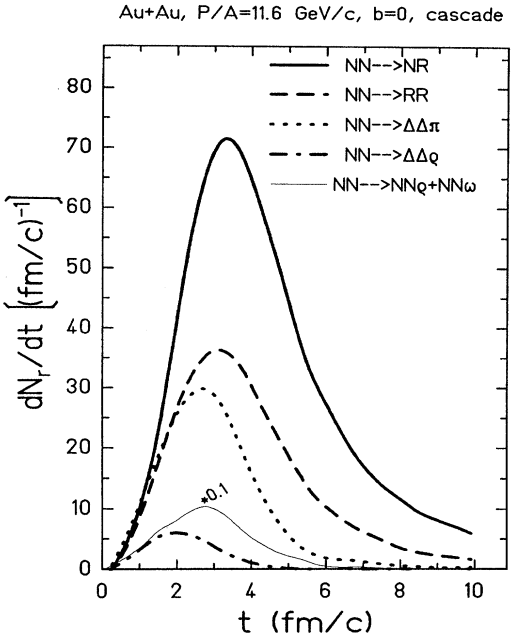

FIG. 12. Reaction rates for various channels in nucleon +nucleon collisions as functions of time in head-on collisions of Au+Au at $p_{\text{beam}}/A = 11.6$ GeV/c.

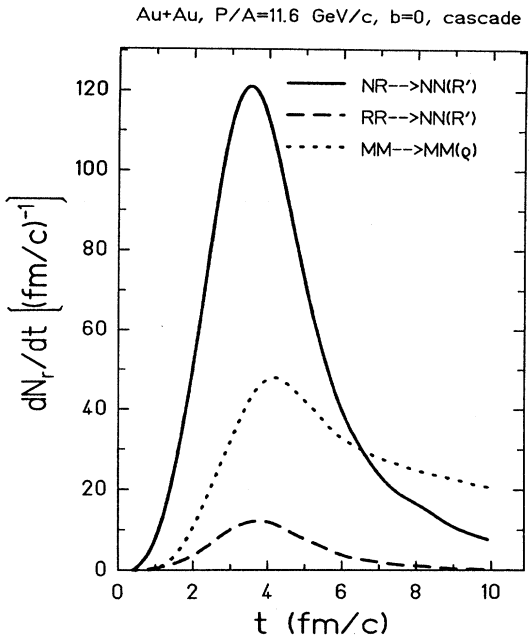

FIG. 13. Reaction rates of nucleon+baryon resonance, baryon resonance+baryon resonance, and meson+meson collisions as functions of time in head-on collisions of Au+Au at $p_{\text{beam}}/A = 11.6$ GeV/c.

Moreover, hadronic models are useful for studying in-medium properties of hadrons. Theoretical studies (e.g., [44–47]) have shown that the properties of hadrons, such as the mass and decay width, may be modified in hot dense hadronic matter as a result of the partial restoration of chiral symmetry. In the following, we shall apply the present model to study several general, but important aspects and issues of heavy-ion collisions at AGS energies. In the subsequent work we plan to study among many other subjects: (i) the effects of changing hadron properties in hot dense medium on heavy-ion collision dynamics and, in particular, on the production of exotic particles, (ii) the beam energy dependence of the collision dynamics from 2 GeV/nucleon up to AGS energies which will be carried out experimentally by the EOS collaboration, and (iii) the role of quark and gluon degrees of freedom at high densities and the study of physics related to the phase transition to the QGP.

A. Reaction dynamics at AGS energies

To study the reaction dynamics of central heavy-ion collisions at AGS energies, we shall first study in this section the reaction rates of various hadron-hadron collisions. To avoid the complexity introduced by the mean field, we shall use the cascade mode of ART. In particular, we shall consider head-on collisions of Au+Au at $p_{\text{beam}}/A = 11.6$ GeV/c as an example for discussions.

Figure 12 shows the reaction rates of nucleon-nucleon scattering to the final states NR, RR, $\Delta\Delta\pi$, $NN\rho$, and $NN\omega$ where R denotes baryon resonances Δ, $N^*(1440)$, or $N^*(1535)$. As one would expect from the decomposition of the total inelastic cross sections discussed in the previous section, the rate of the quasi-3π channel is the highest at the very beginning of the reaction when $t \leq 1$ fm/c, but is closely followed by the quasi-2π and quasi-1π channels. Since particles lose their energies after several collisions, the single-baryon resonance production soon becomes dominant. The collision rates for producing ρ and ω are, however, about an order of magnitude smaller than the quasi-4π channel. Most collisions cease after about 10 fm/c except the single-resonance production channel $NN \rightarrow NR$ which lasts a little longer. For comparison, it is worth noting that the maximum reaction rate reached in the collision is about an order of magnitude higher than that in heavy-ion collisions at Bevalac and SIS-GSI energies [12,48].

The rescattering or absorption of produced baryon resonances and mesons are very important in heavy-ion reactions at AGS energies. In Fig. 13 we show the reaction rates for nucleon+resonance, resonance+resonance, and meson +meson scattering. It is seen that the nucleon+resonance scattering starts earlier and dominates during most of the collision time. The meson+meson and resonance+resonance rescattering starts later as it takes some time to create these secondary particles. After about 10 fm/c the nucleon +resonance and resonance+resonance scatterings are almost over. One also notices that meson+meson scattering lasts longer mainly due to the large $\pi+\pi$ elastic cross section, although the rate decreases towards the later time of the collision. All these features are what one would expect and easily understandable. The relatively low rate for baryon resonance+baryon resonance collisions needs, however, some explanations. The most important reason is that the

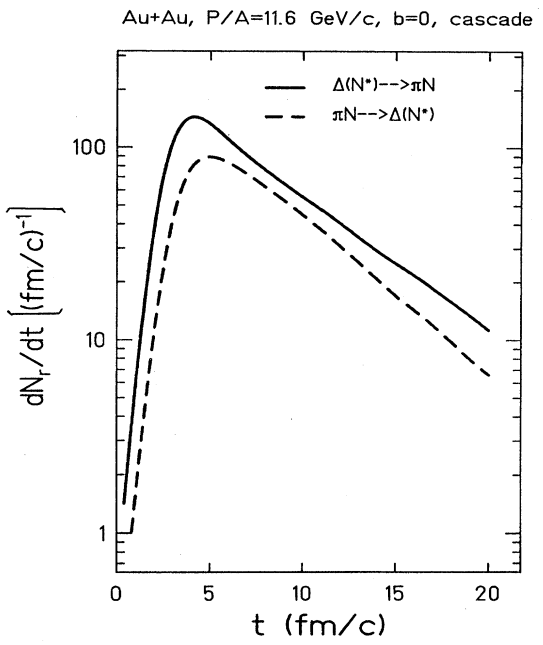

FIG. 14. Rates of baryon resonance decays and formations in meson+baryon collisions as functions of time in head-on collisions of Au+Au at $p_{\text{beam}}/A = 11.6$ GeV/c.

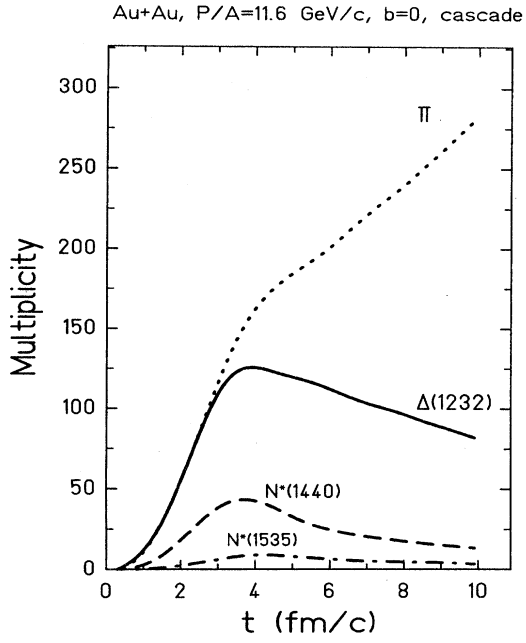

FIG. 15. The evolution of the π, Δ, and N^* multiplicities in head-on collisions of Au+Au at $p_{\text{beam}}/A = 11.6$ GeV/c.

final states in resonance+resonance collisions are limited only to NN, NR', and K^+X in the present version of the model, instead of allowing for the production of up to four quasipions as in nucleon+nucleon collisions. In addition, due to the large spin degeneracy in the initial state, the cross sections obtained from the detailed balance relation for the $RR \rightarrow NN(R')$ reactions are relatively small compared to their reverse reactions.

In Fig. 14, we show the decay rate of baryon resonances together with their formation rate from $\pi+N$ collisions. An interesting feature of these rates is that they last a longer time than hadron+hadron collisions due to the large meson +baryon cross sections. Another feature is that the small difference between the rates of decay and formation of baryon resonances makes the apparent lifetimes of these resonances much longer than their lifetimes in free space. This is rather clear from the evolution of the pion and baryon resonance multiplicities shown in Fig. 15. It is also seen that about half of the baryons are in their excited states at about 4 fm/c, which is the instant of the highest compression as we will discuss in the next section. The abundance of baryon resonances is dominated by $\Delta(1232)$ resonances as one would expect in this energy range. However, it should be stressed that the population of $N^*(1440)$ and $N^*(1535)$ resonances is also significant. These higher resonances serve as an energy reservoir and thus play an important role in the production of particles, especially those having higher energy thresholds [49]. It is also interesting to note that the number of pionlike particles (free pions + baryon and meson resonances) is about the same as the initial number of resonances at the time of maximum compression.

In Fig. 16, we show the time-integrated total number of hadron-hadron collisions as a function of the center-of-mass energy $\sqrt{s}$ of the colliding pairs for $N+N$, $N+R$, $R+R$, $M+B$, and MM collisions, where the meson+baryon $(M+B)$ and meson+meson $(M+M)$ collisions include contributions from both baryon and meson resonances. It is seen that $N+N$ collisions start at about $\sqrt{s}=1.8$ GeV and peak at about $\sqrt{s}=2.2$ GeV. The peak is mainly due to the large number of elastic scattering. The position of the peak shifts to higher energies and its hight decreases substantially in $N+R$ and $R+R$ reactions. The reasons are mainly the following. First of all, we have assumed that the elastic cross sections for $N+R$ and $R+R$ collisions are the same as for $N+N$ collisions at the same center-of-mass energy $\sqrt{s}$. Since the elastic cross section decreases quickly as the center-of-mass energy increases, the heavier masses of the baryon resonances then result in smaller elastic cross sections for

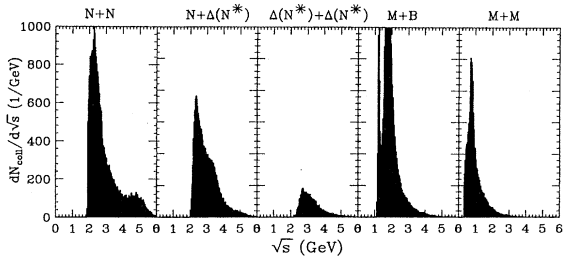

FIG. 16. Collision number distributions as functions of center-of-mass energy in head-on collisions of Au+Au at $p_{\text{beam}}/A = 11.6$ GeV/c.

$N+R$ and $R+R$ collisions. In addition, as we have mentioned earlier, the number of final states in $N+R$ and $R+R$ collisions are reduced compared to that in $N+N$ collisions. For meson+baryon reactions, the collision number distribution have two distinct peaks at $\sqrt{s}\approx 1.2$ GeV and $\sqrt{s}\approx 2$ GeV, respectively. The first peak apparently corresponds to the formation of the $\Delta(1232)$ resonance, while the second peak has contributions also from the N^* resonance and direct π-N collisions. The meson+meson collision number has a peak at about the ρ mass $\sqrt{s}\approx m_\rho = 0.77$ GeV.

The above examination on the collision dynamics indicates that the model is working well under control, regardless of the question whether some of the assumptions made in the model can be improved. This gives us further confidence about the model.

B. Formation of superdense hadronic matter

Depending on the nature of the quark-gluon plasma phase transition at high baryon densities, the crossover energy between the hadronic and quark-gluon phases may occur anywhere between $E_{\rm lab}/A = 2$ and 10 GeV [50,51]. It was pointed out recently that the current Au+Au reactions at 11.6 GeV/c may have already overshot the transition region [52]. It is therefore of great interest to critically examine the baryon, meson, and energy densities reached in these collisions. In this section, we study the local baryon, meson, and energy densities in head-on collisions of Au+Au at $p_{\rm beam}/A = 11.6$ GeV. It will be shown that in these collisions a superdense hadronic matter with a density higher than the critical density for the phase transition can be formed in a sufficiently large volume and for a sufficiently long time. We will also study the dependence of the size and lifetime of the superdense hadronic matter on the nuclear mean field.

The standard test particle method [53] is used to calculate the global density ρ_g in the nucleus-nucleus c.m. frame on a lattice of size 40-40-48 with a volume of 1 fm^3 for each cell. In the test particle method, one replaces the continuous phase-space distribution function with a finite number of test particles representing individual phase space cells, i.e.,

$$f(\mathbf{r},\mathbf{p},t) \simeq \frac{1}{N_t}\sum_i \delta(\mathbf{r}-\mathbf{r}_i(t))\delta(\mathbf{p}-\mathbf{p}_i(t)), \tag{93}$$

where $\mathbf{r}_i$ and $\mathbf{p}_i$ are the coordinates and momenta of the test particles. N_t is the number of test particles per nucleon; we usually use $N_t = 100$ for Au+Au collisions. The global baryon, meson, and energy density functions ρ_g^b, ρ_g^m, and e_g are evaluated via

$$\rho_g^b(r,t) = \sum_{i=N,\Lambda,\Sigma} \int \frac{d^3\mathbf{p}}{(2\pi)^3} f_i(\mathbf{r},\mathbf{p},t) + \sum_{i=\Delta,N^*} \int \frac{d^3\mathbf{p}}{(2\pi)^3}\frac{dm}{2\pi} f_i(\mathbf{r},\mathbf{p},t), \tag{94}$$

$$\rho_g^m(r,t) = \sum_{i=\pi,K,\eta,\omega} \int \frac{d^3\mathbf{p}}{(2\pi)^3} f_i(\mathbf{r},\mathbf{p},t) + \int \frac{d^3\mathbf{p}}{(2\pi)^3}\frac{dm}{2\pi} f_\rho(\mathbf{r},\mathbf{p},t), \tag{95}$$

$$e_g(r,t) = \sum_i \int \frac{d^3\mathbf{p}}{(2\pi)^3}(p^2+m^2)^{1/2} f_i(\mathbf{r},\mathbf{p},t) + \sum_j \int \frac{d^3\mathbf{p}}{(2\pi)^3}\frac{dm}{2\pi}(p^2+m^2)^{1/2} f_j(\mathbf{r},\mathbf{p},t). \tag{96}$$

In the last equation, i runs over all particles with fixed masses while j runs over all particles with variable masses.

The local baryon, meson, and energy densities in each cell are then obtained from $\rho_l^b = \rho_g^b/\gamma$, $\rho_l^m = \rho_g^m/\gamma$, and $e_l = e_g/\gamma$, where γ is the Lorentz factor of each cell,

$$\gamma = \sum_i E_i \Big/ \sqrt{\Big(\sum_i E_i\Big)^2 - \Big(\sum_i \vec{p}_i\Big)^2}. \tag{97}$$

In the above, i runs over all particles in the cell. For most parts of the colliding nuclei, the use of local densities can eliminate the trivial compression effects due to the initial Lorentz contraction of the two nuclei. However, in the most central cell where the two nuclei are in touch and streaming towards each other, the γ factor is almost 1. Therefore, we have at the very beginning of the collision, $\rho_l^b \approx \rho_g^b = 2\gamma_0\rho_0$ where γ_0 is the center-of-mass Lorentz factor of the colliding nuclei, and for Au+Au at $P_{\rm beam} = 11.6$ GeV/c, one has $\gamma_0 = 2.6$. Fortunately, this initial high baryon density is only in a very small region at the very beginning and is soon destroyed by the violent collisions that follow. In the cascade model calculations, the initial high baryon density in the most central cell is simply a matter of presentation. For calculations including the density-dependent mean field we have found from comparisons with calculations using the scalar density that the initial high baryon density has no ef-

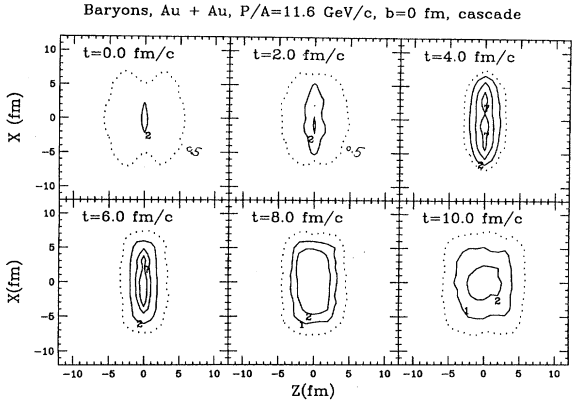

FIG. 17. The evolution of local baryon density in the reaction plane in head-on collisions of Au+Au at $p_{\rm beam}/A = 11.6$ GeV/c.

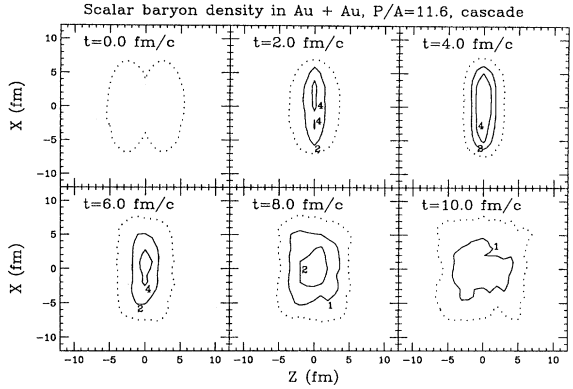

FIG. 18. Same as Fig. 17 for the scalar baryon density.

fects on the collision dynamics and the final observables.

We show in Fig. 17 the evolution of the local baryon density distribution in the reaction plane using the cascade mode of ART 1.0 for the head-on collision of Au+Au at $P_{\rm beam}/A = 11.6$ GeV/c. The outmost contour is for $\rho_l = 0.5\rho_0$, and the numbers in the figure are the densities of the corresponding contours in units of ρ_0. The two Lorentz contracted nuclei are set in touch at $t=0$. It is seen that the initial high density region bounded by the contour with $\rho = 2\rho_0$ is very small. The two nuclei soon form a compressed disk and reach the maximum compression of about $9\rho_0$ at about 4 fm/c. The compressed hadronic matter then starts to expand at about 6 fm/c. We see that up to 10 fm/c the longitudinal expansion is significantly stronger than the transverse one. This observation seems to indicate that the isotropically expanding, spherical fireball model widely used for describing heavy-ion collisions at AGS energies may need to be improved. It should be mentioned that the main features observed here are in general agreement with those extracted from the ARC calculations [3].

The local densities are well defined and are the relevant quantities for discussing the interesting physics of the phase transition to a quark-gluon plasma. However, the current model is still not fully relativistically covariant. To estimate the minimum compression reached during the collision for a given system at a fixed beam energy and impact parameter, we show in Fig. 18 the scalar baryon density ρ_s^b defined as

$$\rho_s^b(r,t) = \sum_{i=N,\Lambda,\Sigma} \int \frac{d^3\mathbf{p}}{(2\pi)^3} f_i(\mathbf{r},\mathbf{p},t) \frac{m}{e} + \sum_{i=\Delta,N^*} \int \frac{d^3\mathbf{p}}{(2\pi)^3} \frac{dm}{2\pi} f_i(\mathbf{r},\mathbf{p},t) \frac{m}{e}, \tag{98}$$

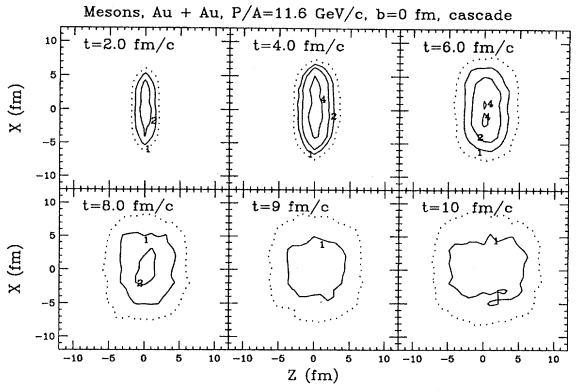

FIG. 19. Same as Fig. 17 for the local meson density.

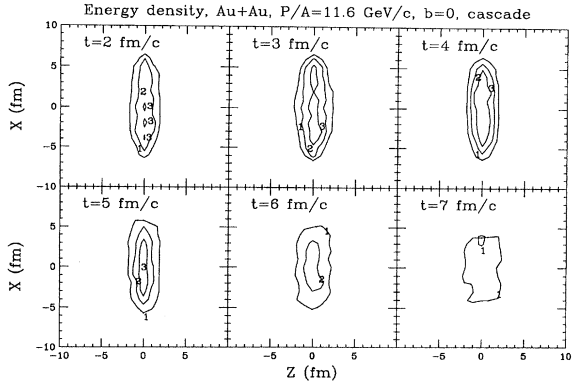

FIG. 20. Same as Fig. 17 for the local energy density.

where e is the energy of a baryon. In the limit that the size of each cell is very small such that it can only accommodate one particle the local density becomes equal to the scalar density. It is seen that the main features in the evolution of the scalar density are similar to those of the local density. It is interesting to note that the initial high density region around the most central cell in the local density plot does not appear here as one would expect. We have found that the maximum scalar density reached at 4 fm/c is about $6.5\rho_0$ which is significantly smaller than the maximum local density reached in the collision.

The local density of mesons (mostly pions) can be as high as that of nucleons during the collision. The evolution of the meson density distribution in the reaction plane is shown in Fig. 19. Mesons mainly populate the central region for $t \leq 2$ fm/c, and they spread out quickly soon after that and finally occupy the whole collision volume. The maximum meson density of about $4.5\rho_0$ is reached at about 4 fm/c. As we have discussed earlier, at this time about half of final pions are still bound in resonances. It is also interesting to see that mesons start to expand earlier and faster than baryons. After about 8 fm/c, the meson sector of the system has already been expanding almost isotropically. In principle, the geometry and time scale of the expanding hadronic matter studied here can be compared directly with the interferometry measurements to further test the model.

To form a quark-gluon plasma, it is necessary to achieve a high local energy density in a sufficiently large volume and for a sufficiently long time such that the initial plasma droplets can grow. The current estimate for the critical baryon and energy densities at which the QGP may form are about $5\rho_0$ and 2.5 GeV/fm^3, respectively [30]. From the above studies on the baryon and meson densities, we have seen that the superdense hadronic matter occupies a large volume and for a rather long time. As to the possible phase transition to the quark-gluon plasma, more complete and quantitative information about the local energy density of the superdense hadronic matter are needed. Figure 20 shows the evolution of the local energy density in the reaction plane for the head-on collision of Au+Au at $p_{\text{beam}} = 11.6$ GeV/c. The numbers in the figure are the energy densities in units of GeV/fm^3. It is seen that a small, thin disk of energy density higher than 2.5 GeV/fm^3 has already been formed at about 2.0 fm/c. It grows until about 4 fm/c, then starts to decay, and at about 7 fm/c it disappears due to expansions. The superdense hadronic matter has thus a lifetime of about 5 fm/c and a maximum volume of about 200 fm^3 at about 4 fm/c.

The results obtained from the cascade calculations seem to indicate that in head-on collisions of Au+Au at $p_{\text{beam}}/A = 11.6$ GeV/c, the conditions for forming a quark-gluon plasma has indeed been reached. However, this also marks the breakdown of the hadronic models and the need to include new degrees of freedom. It is thus a great challenge to actually convert this superdense hadronic matter into the quark-gluon plasma. Without introducing explicitly the quark and gluon degrees of freedom in the model make this impossible. Nevertheless, before one can study the properties of the quark-gluon plasma, it is necessary to investigate how and to what degree the properties of the superdense hadronic matter may be affected by the nuclear mean field, which is an important piece of physics neglected in cascade calculations. In the following, we shall compare results obtained with and without the mean field.

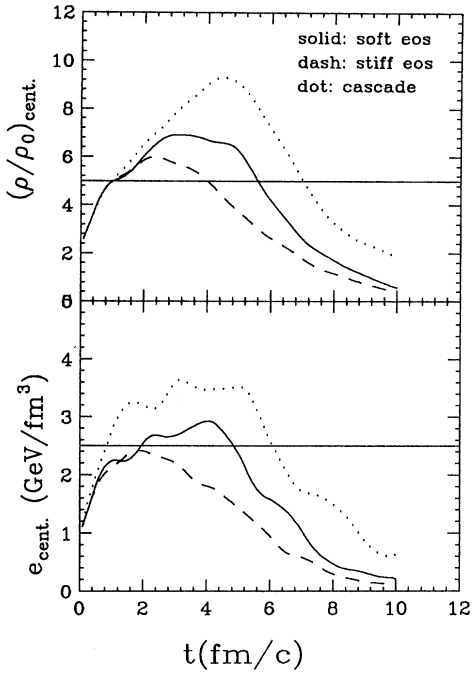

FIG. 21. The evolution of central local baryon and energy densities in the collision of Au+Au at $P_{\text{beam}}/A = 11.6$ GeV/c and $b = 0$ calculated with the cascade, the soft, and the stiff equations of state.

First of all, we have found that the general features in the evolution of the baryon, meson, and energy density distributions are very similar in the two calculations. However, important quantitative differences exist. Figure 21 shows the evolution of the local baryon and energy densities in the most central cell during the collision of Au+Au at $P_{\text{beam}}/A = 11.6$ GeV/c and $b = 0$. Results from the cascade calculations are compared with those from calculations using the soft nuclear equation of state with $K = 200$ MeV and the stiff one with $K = 380$ MeV. As expected, the mean field has almost no effect in the early stage of the collision when the kinetic energy is much higher than the potential energy. Significant differences appear soon after about 2 fm/c. In the cascade case, it is seen that a maximum baryon density of about $9\rho_0$ and a maximum energy density of about 3.6 GeV/fm^3 are reached at about 4 fm/c. The matter in the high energy density region lasts for about 5 fm/c. The volume of the high density region are, however, significantly reduced by the repulsive mean field. Furthermore, the lifetime, maximum baryon, and energy densities are reduced to about 3 fm/c, $7\rho_0$, and 2.6 GeV/fm^3, respectively, when using the soft nuclear equation of state. With the stiff equation of state the reduction is even larger. Since the stiff equation of state violates causality already at about $3\rho_0$, we will only use the soft equation of state in the following. The reduction of the maximum baryon and energy densities due to the mean field may be large enough to affect significantly the collision dynamics.

Additional information about the importance of the

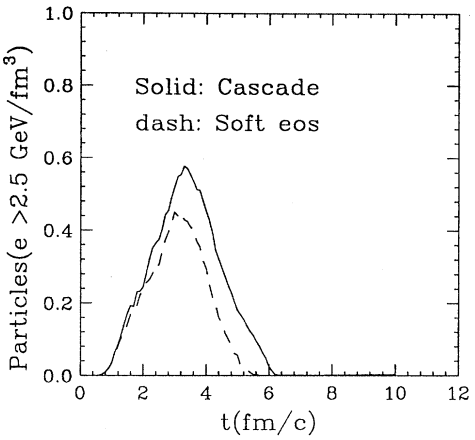

FIG. 22. The evolution of the fraction of particles with local energy density higher than 2.5 GeV/fm^3 in head-on collisions of Au+Au at $P_{\text{beam}}/A = 11.6$ GeV/c.

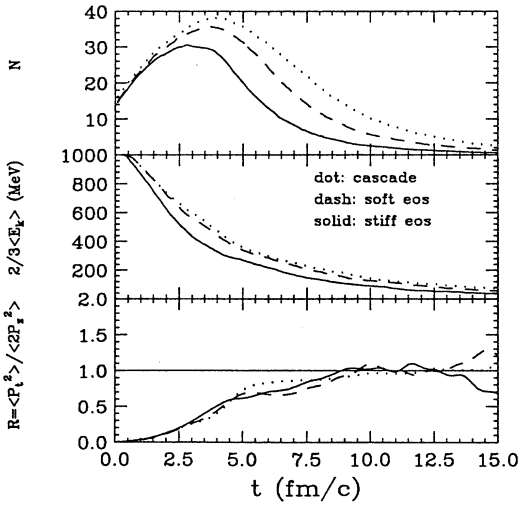

FIG. 23. (Upper window): the evolution of the particle number in a sphere with a radius of 2 fm around the center of mass. (Middle window): the evolution of the average kinetic energy $\langle \frac{2}{3}E_K \rangle$ per particle in the sphere. (Lower window): the evolution of the stopping ratio R in head-on collisions of Au+Au at $P_{\text{beam}}/A = 11.6$ GeV/c.

nuclear mean field can be obtained by comparing the fraction of particles with local energy densities $e_l \geq 2.5$ GeV/fm^3 from calculations with and without the mean field. This is shown in Fig. 22. In the cascade calculation about 60% of particles are in the high energy density region at the instant of the maximum compression. The soft equation of state reduces it to about 30%, and this reduction persists during the expansion phase of the collision.

C. Thermalization and radial flow

To what degree the superdense hadronic system is thermalized and what is the time scale for achieving thermal equilibrium are among the most important questions in heavy-ion collisions at AGS. Answers to these questions are useful both for developing static models and for interpreting the experimental data. For example, in thermodynamic models one usually assumes that there exists a thermalized freeze-out stage when particles in the expanded system cease to strongly interact with each other. In view of the apparent success of the thermodynamical approach (e.g., [54]) in explaining a large amount of data from heavy-ion collisions at AGS energies we study in this section the question of thermalization. In addition, the large thermal and compressional pressure in the superdense hadronic matter is found to induce a radial flow during the expansion phase. This is already qualitatively clear from our discussions in the previous section, and we study here more quantitatively the radial flow.

We consider all hadrons in a sphere of radius 2 fm around the origin in the center-of-mass frame for head-on collisions of Au+Au at $p_{\text{beam}}/A = 11.6$ GeV/c. The degree of thermalization can be measured by the ratio

$$R = \frac{\Sigma_i (p_{ix}^2 + p_{iy}^2)}{2\Sigma_i p_{iz}^2} . \tag{99}$$

Then $R = 1$ is a necessary, although not a sufficient, condition for thermal equilibrium. It is also a measure of the stopping power. In the bottom window of Fig. 23, we show this ratio as a function of time. For all three calculations based on the cascade and the soft and the stiff equations of state, the ratio reaches 1 at about 10 fm/c. From our early discussions on the reaction rates for various channels, it is clear that this is about the time when most hadronic collisions have stopped. It is therefore reasonable to use the concept of thermal equilibrium at the time of freeze-out.

It is interesting to note that at about 4 fm/c when the system reaches its maximum compression the ratio R is about 0.7, indicating that the superdense hadronic system has not reached thermal equilibrium. To estimate the temperature of particles in the above sphere at the time of thermalization, we show in the middle window the scaled average kinetic energy per particle $\langle \frac{2}{3}E_k \rangle$. At freeze-out, this quantity can give a good estimate of the temperature. Before freeze-out, the evolution of this quantity reflects the collision dynamics. It is seen that the kinetic energy decreases quickly in the compression phase due to the creation of baryon resonances and other particles as well as various scattering. In the expansion phase, high energy particles near the surface of the sphere move out continuously due to the radial flow. The average kinetic energy in the sphere thus gradually decreases in the expanse phase. At the time of freeze-out this quantity is about 120 MeV and slightly depends on the model. This value is very close to the temperature extracted from the inverse slope of the measured particle spectra. It is interesting to note that both the time scale for thermalization and the temperature at freeze-out are not very sensitive to the equation of state. However, the temperature from the cascade is about 30 MeV higher than that from calculations with the mean field due to the neglect of the potential energy in the former.

In our calculations, the system has undergone sufficient expansion before reaching thermal equilibrium at freeze-out, and this is in agreement with the conclusion reached from studies of the AGS data based on the thermodynamical

model [54]. More quantitative information about the expansion can be seen from the upper window where the number of particles in the central sphere is plotted as a function of time. General features of this plot are the same as that of the central density plot discussed earlier. It is seen that the number of particles in the sphere at freeze-out is only about 30% of that at the maximum compression indicating a strong expansion before the freeze-out.

The velocity profile of the radial flow at freeze-out can be expressed by

$$\beta(r)=\frac{1}{N_r}\sum_{i=1}^{N_r}\frac{\vec{p}_i}{e_i}\cdot\frac{\vec{r}_i}{r_i}, \tag{100}$$

where N_r is the number of particles in a spherical shell of size $\Delta r=0.5$ fm at a radius r. The momentum $\vec{p}_i$ of each particle has a flow component and a random thermal component:

$$\vec{p}_i=\vec{p}_{if}+\vec{p}_{it}. \tag{101}$$

In the limit that there is a large number of particles in each shell, the summation in Eq. (100) cancels out the thermal part, i.e.,

$$\sum_{i=1}^{N_r=\infty}\frac{\vec{p}_{it}}{e_i}\cdot\frac{\vec{r}_i}{r_i}=0, \tag{102}$$

and Eq. (100) reduces thus to the flow velocity $\beta_f(r)$,

$$\beta(r)\approx\beta_f(r)=\sum_{i=1}^{N_r=\infty}\frac{\vec{p}_{if}}{e_i}\cdot\frac{\vec{r}_i}{r_i}. \tag{103}$$

Since we usually use a large number of test particles, Eq. (100) gives a good estimate of the radial flow profile. In Fig. 24, we show the estimated flow profile and the corresponding radial density distributions for baryons and pions. The left window is for the cascade and the right one is for calculations using the soft equation of state. The radial flow velocity is proportional to the radius, but there seem to be two distinct slopes at radii smaller and larger than about 6 fm. Another interesting feature is that pions seem to flow a little faster than baryons due to their lighter masses. It is also seen that the difference between the flow profiles from calculations with and without the mean field is rather small, which may indicate that the thermal pressure dominates at freeze-out. As seen from the upper window, more particles are at larger radii due to the repulsive mean field, so more energy are stored in the radial flow in the case with the mean field.

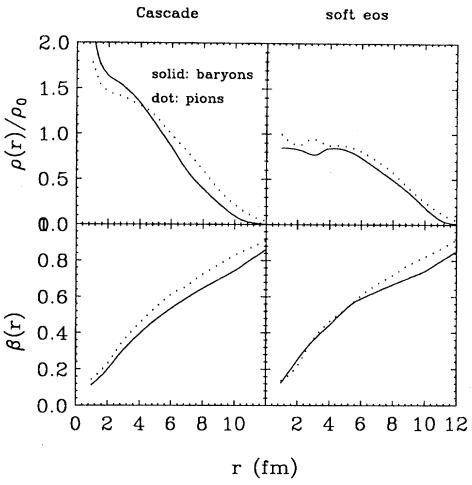

FIG. 24. (Upper windows): Radial density distributions for baryons and pions at freeze-out calculated using the cascade (left) and the soft equation of state (right). (Lower windows): the radial flow velocity profiles at freeze-out in head-on collisions of Au+Au at $P_{\text{beam}}/A=11.6$ GeV/c.

For comparisons, we mention here that results of a recent hydrodynamical model analysis of a large amount of data from central collisions of Si+Au at $p_{\text{beam}}/A=14.6$ GeV/c are consistent with the above discussions. Assuming a freeze-out radius of about 7 fm, a freeze-out temperature of 120 (140) MeV, and a linear flow velocity profile, the extracted maximum flow velocity is about $0.58c$ ($0.5c$) [54], which agrees with the flow profile we have extracted.

D. Stopping power and inclusive observables

The formation of a quark-gluon plasma or a mixed phase of hadrons, quarks, and gluons is expected to reduce the pressure of the system and leads to a softened equation of state. It is therefore interesting to search for experimental

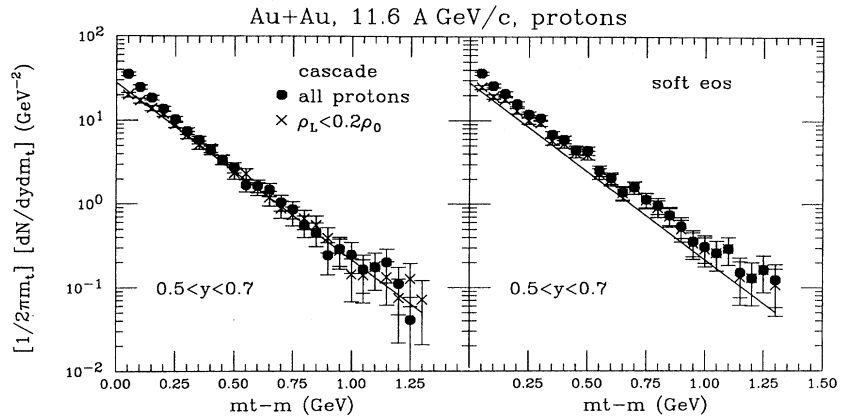

FIG. 25. Transverse momentum distributions of protons in the collision of Au+Au at $P_{\text{beam}}/A=11.6$ GeV/c and at an impact parameter of 2 fm. The solid line is the least squares fit to preliminary data from the E802 Collaboration. See discussions in the text.

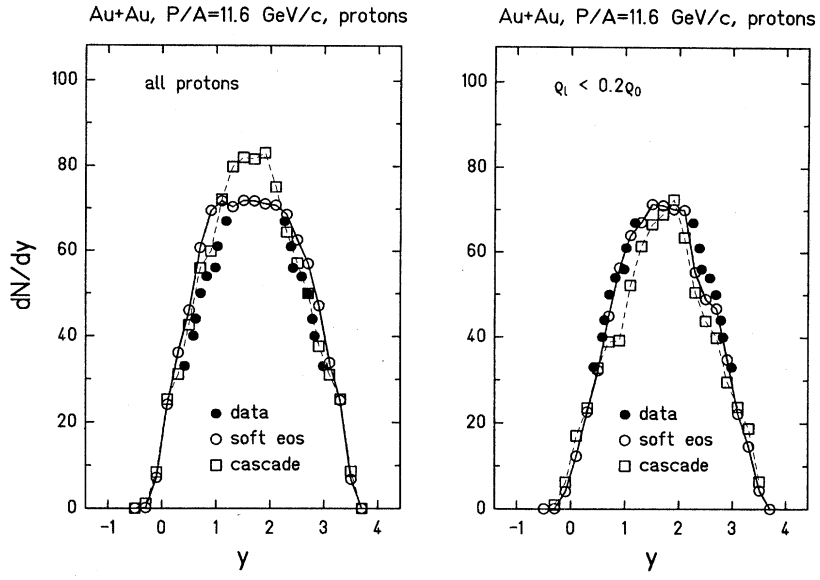

FIG. 26. Rapidity distributions of protons in the collision of Au+Au at $P_{\text{beam}}/A = 11.6$ GeV/c and at an impact parameter of 2 fm.

observables that are sensitive to the nuclear equation of state. In this section, we study the sensitivity of inclusive, single-particle observables to the equation of state by comparing calculations with and without the mean field. However, we should mention again that present models for heavy-ion collisions at AGS energies are probably inconsistent. Namely, we have shown in the above that the conditions for forming the quark-gluon plasma may have been fulfilled in central collisions at AGS energies. Without actually including the phase transition to the quark-gluon plasma and the hadronization back to the hadronic phase in the model, we are limited to discuss only the hadronic physics.

Specifically, we shall study the rapidity and transverse momentum distributions of protons and pions. We leave the study of kaon distributions to the next section in central collisions of Au+Au at $p_{\text{beam}}/A = 11.6$ GeV/c. For references, we also compare with preliminary data from the E802/E866 Collaboration [55]. These data were taken using the kinetic energy in the zero degree calorimeter as a trigger on the impact parameter. The data for central collisions roughly correspond to the upper 4% of the total cross section or impact parameters smaller than about 3 fm. Since the data still have a 15% systematic errors besides the statistical ones, we have not let the generated events going through the zero degree calorimeter to simulate the experimental trigger conditions. Instead, we perform calculations with impact parameters smaller than 3 fm and compare the data with calculations using the impact parameter of 2 fm which is about the average impact parameter of the central collisions. This is probably sufficient for our current purposes.

First, let us study the proton transverse momentum distribution. In Fig. 25, we show the calculated spectrum by the round symbols in the left window using the cascade and the right window using the soft equation of state. The least squares fit to the data of Ref. [55] is shown by the solid lines. In the cascade case, the calculation agrees with the data rather well except in the low transverse momentum region. The larger theoretical values are probably due to the fact that we count all protons in the final state although some of them are still bound in light clusters, while the data are for protons only. To estimate the number of bound protons, we apply a cut to the local baryon density such that only protons with $\rho_l < 0.2\rho_0$ are counted. The spectra calculated in this way are shown with the cross symbols which agree well with the data even at low transverse momenta. The spectra calculated with the soft equation of state show an increase of about 25% mainly at large transverse momenta compared with that from the cascade as a result of the repulsive mean field at high densities. This difference, however, is comparable to the combined statistical and systematical errors of the data. Nevertheless, it is promising that the proton spectra at high transverse momenta may be useful for studying the equation of state at the level of sensitivity of about 25%. As we will show later, a much clearer sensitivity at the level of 250% can be obtained from an event by event analysis of the baryon transverse collective flow.

In Fig. 26, we show the calculated proton rapidity distri-

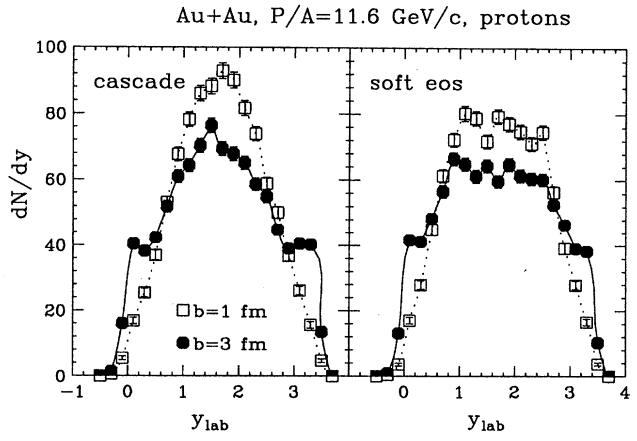

FIG. 27. Comparison of rapidity distributions of protons in the collision of Au+Au at $P_{\text{beam}}/A = 11.6$ GeV/c and at impact parameters of 1 and 3 fm.

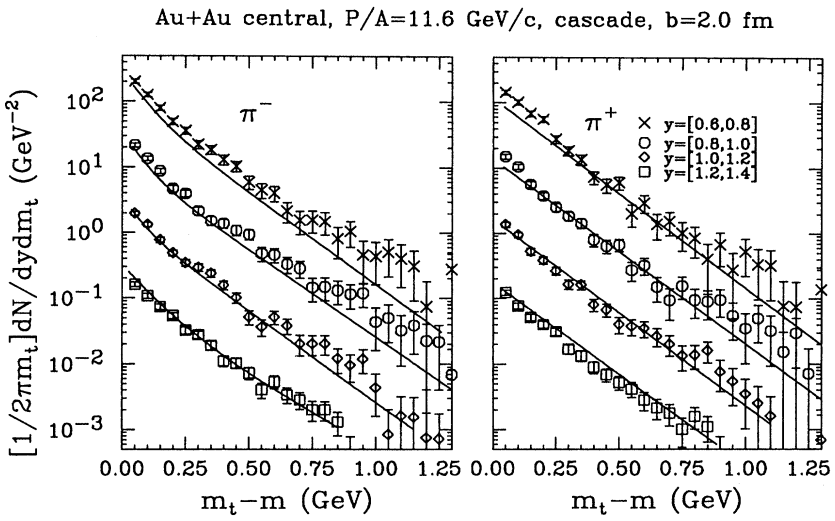

FIG. 28. Transverse momentum distributions of pions from the cascade model for Au+Au collisions at $P_{\text{beam}}/A = 11.6$ GeV/c and at an impact parameter of 2 fm. Solid lines are least squares fits to preliminary data from the E802/E866 collaboration.

butions. As one would expect, the mean field leads to less stopping. This observation is consistent with our early discussions about the mean field effects on the creation of superdense hadronic matter. It is seen that without applying the local density cut at $0.2\rho_0$, the mean field reduces the height but increases the width of dN/dy at midrapidity by about 15%. With the local density cut, the calculation with the mean field can better reproduce the data, but again the difference between the two calculations is comparable to current systematic errors in the data. As we have stated earlier, the above calculations are carried out at a fixed impact parameter of 2 fm. To quantify the impact parameter dependence of the stopping power in central collisions, we show in Fig. 27 the proton rapidity distributions at impact parameters of 1 fm and 3 fm. In both calculations with and without the mean field, the height of the rapidity distribution at the midrapidity increases by about 25% as the impact parameter changes from 3 fm to 1 fm. With an impact parameter of 3 fm, a clear bump due to spectators at the projectile and target rapidities can be seen. The variation of the rapidity distribution at these two impact parameters caused by the mean field is again at the level of 15%.

Pions are copiously produced in heavy-ion collisions at AGS energies and are expected to play an important role in the stopping and thermal equilibration of the system. The study of pion rapidity and transverse momentum spectra provides thus useful information about the collision dynamics, the properties of the superdense hadronic matter, and the particle production mechanisms. In Fig. 28 and Fig. 29, we compare calculated π^+ and π^- transverse momentum spectra using the cascade and soft equation of state with each other and also with the least square fit to the data (solid lines). The rapidity range for each spectrum is indicated in the figure. It is seen that both calculations can reproduce the data reasonably well except at rapidities far from the center-of-mass rapidity, which is about 1.6 for the Au+Au reaction at $p_{\text{beam}}/A = 11.6$ GeV/c. Again, the variation between calculations using the cascade and the soft equation of state is on the order of 20% which is comparable to current experimental errors. The statistics in the calculations can be

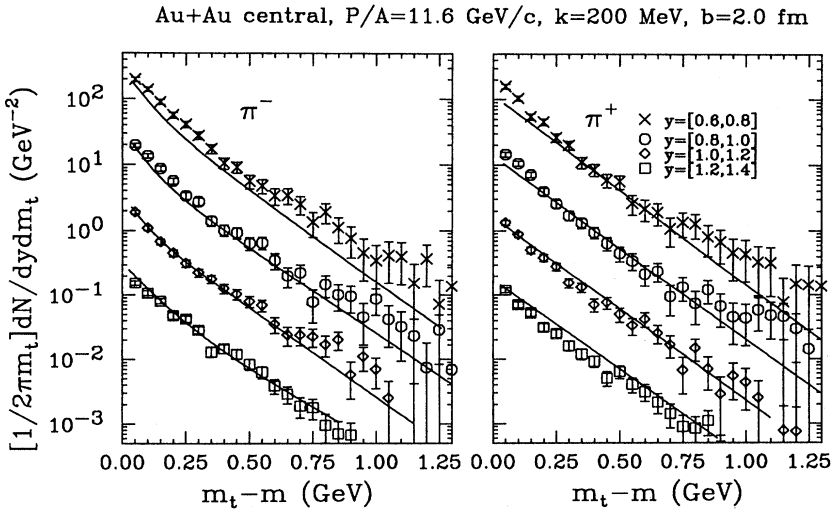

FIG. 29. Same as Fig. 28 for transverse momentum distributions of pions calculated using the soft equation of state.

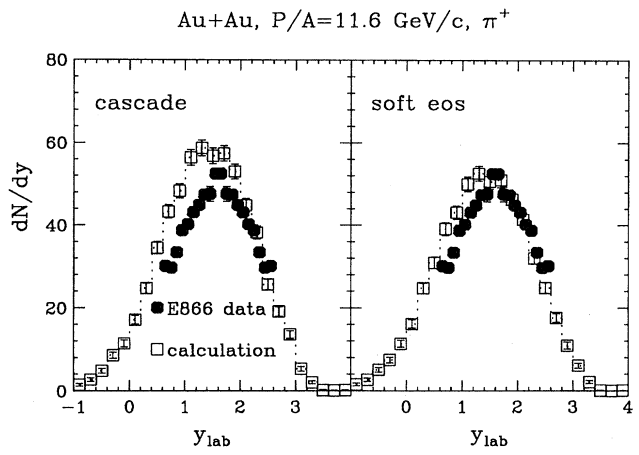

FIG. 30. Rapidity distributions of π^+ in the collision of Au+Au at $P_{\text{beam}}/A = 11.6$ GeV/c at an impact parameter of 2 fm.

significantly improved by mixing events from different impact parameters. But main features of the spectra are expected to remain unchanged. We will leave a more detailed study on pion spectra, including the contribution of resonance decays at freeze-out and the Coulomb effects on the difference between π^+ and π^- spectra to a separate paper.

In Fig. 30, we compare the rapidity distributions of π^+ calculated at an impact parameter of 2 fm using the cascade and the soft equation of state with the experimental data. The calculation with the soft equation of state seems to be closer to the data, but there exists some discrepancies. It is worth mentioning that the experimental rapidity distribution was obtained by first fitting the transverse momentum spectra with an exponential function or a sum of two exponential functions and then extrapolating and integrating over the whole rapidity range. While in our calculations we simply count pions in each rapidity bin without any possible bias from the extrapolation process. It is seen that the difference between calculations with and without the mean field is

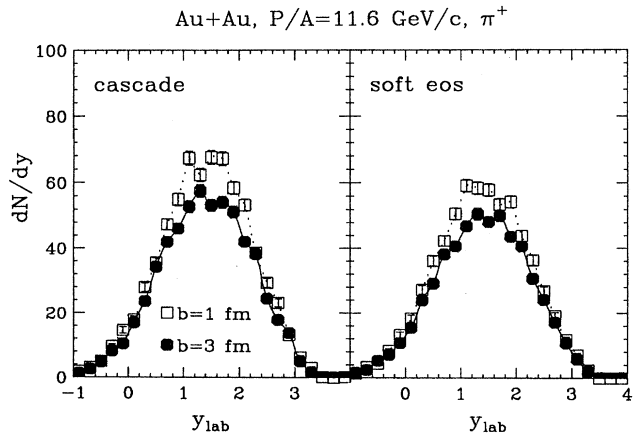

FIG. 31. Comparison of rapidity distributions of π^+ in the collision of Au+Au at $P_{\text{beam}}/A = 11.6$ GeV/c and at impact parameters of 1 and 3 fm.

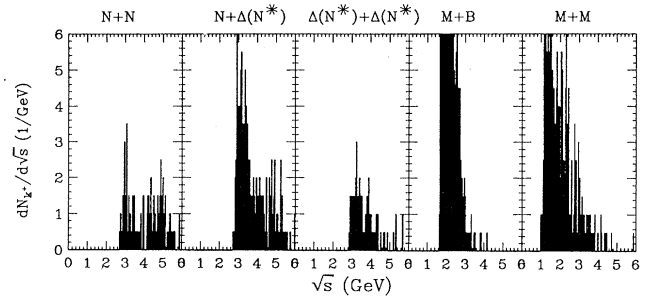

FIG. 32. Energy distributions of K^+ producing collisions as functions of center-of-mass energy in head-on collisions of Au+Au at $p_{\text{beam}}/A = 11.6$ GeV/c.

again on the order of 20%, which is rather similar to the situation at the Bevalac or SIS/GSI energies [17,43]. The impact parameter dependence of the pion rapidity distribution is shown in Fig. 31. The dependence here is rather weak compared to that of the proton rapidity distribution. This is mainly due to the fact that there is an almost complete overlapping between the target and the project in collisions with impact parameters smaller than 3 fm and the large number of pions produced in these collisions.

E. Mechanisms for K^+ production

Mechanisms for kaon production at AGS energies have been a subject of intensive studies in the past few years. In particular, the enhancement of K^+/π^+ ratio in heavy-ion collisions with respect to pp and pA reactions has been attracting much attention due to the possible role of strangeness as a signature of the quark-gluon plasma [56,57]. However, no definite conclusion has been reached due to the complexity of the collision dynamics at AGS energies and our incomplete knowledge about the properties of hadrons and their interactions in hot dense matter.

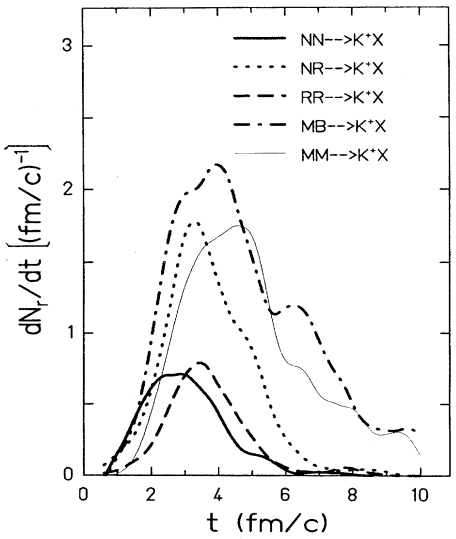

FIG. 33. The evolution of K^+ production rates in head-on collisions of Au+Au at $p_{\text{beam}}/A = 11.6$ GeV/c.

In Fig. 32, we show the contributions to K^+ production from various collision channels as a function of the center-of-mass energy of the colliding pairs in Au+Au collisions at $P_{\text{beam}}/A = 11.6$ GeV/c. It is seen that large contributions come from meson+baryon and meson+meson collisions, besides that from baryon+baryon collisions. This is in agreement with the predictions from Ref. [23] based on the hydrochemical model calculations. More quantitatively, about 35%, 40%, and 25% of the produced kaons come from baryon+baryon, meson+baryon, and meson+meson collisions, respectively. The relative importance of different K^+ sources seen here does not agree completely with results from either the RQMD or the ARC. Since there are many assumptions in each model, it is not apparent to us at this time what is the cause for the difference among these models. It is certainly of great interest to resolve this difference in future studies. However, this can only be possible when all assumptions used in all models are made clear.

For ease of future comparisons with other models and also for studying the kaon production dynamics, we show in Fig. 33 the K^+ production rate as a function of time for various channels. The calculation is carried out for head-on collisions at $p_{\text{beam}}/A = 11.6$ GeV/c using the cascade. It is seen that at $t \approx 1.0$ fm/c the production rates due to nucleon +nucleon, meson+baryon (including resonances), and nucleon+baryon resonance are almost the same. Soon after that the K^+ production rate is dominated by meson+baryon collisions which also last a longer time. The K^+ production rates due to nucleon+baryon resonance, nucleon+nucleon, and baryon resonance+baryon resonance decrease to zero after about 6 fm/c. Meson+meson collisions come in later, but they contribute significantly to the K^+ production especially during the expansion phase of the collision. The time dependence of K^+ production studied here may be useful for further studies on the production mechanisms for kaons. Moreover, kaons produced at different times through different channels may also contribute to different parts of the kaon spectra. We, however, leave the more detailed discussions on this subject to future studies.

We now go back to the question of comparing kaon spectra calculated with and without the mean field with the preliminary data from the E802/E866 collaboration. Figure 34 shows the comparison on the kaon transverse momentum distributions. The solid lines in both windows are the exponential fit to the data to guide the eye. It is seen that both calculations agree with the data reasonably well. However, there are some discrepancies between calculations and experimental data especially at high transverse momenta. Within error bars of the calculations the two calculated spectra are almost indistinguishable. Figure 35 shows the K^+ rapidity distributions. The data at rapidities larger than 1.6 are the reflections of those at rapidities less than 1.6. Except at rapidities near the center-of-mass rapidity the two calculations are very close to each other. Even at the midrapidity the sensitivity to the equation of state is only about 15%. This situation is rather different from that at SIS-GSI energies where subthreshold kaon production is very sensitive to the nuclear equation of state [58–62]. Since kaon production at AGS energies is high above the threshold, the sensitivity of kaons to the equation of state is not expected to be very different from that of nucleons and pions. To be complete,

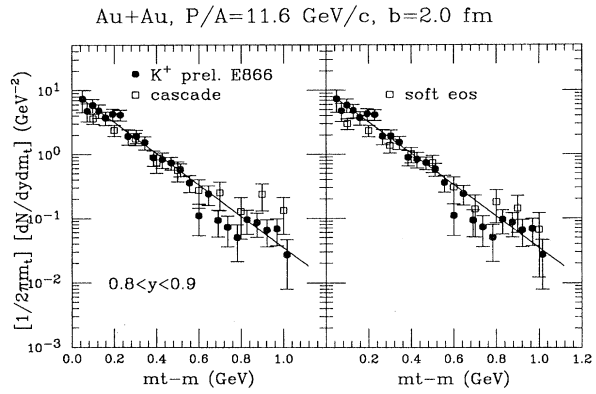

FIG. 34. Transverse momentum distributions of K^+ in the collision of Au+Au at $P_{\text{beam}}/A = 11.6$ GeV/c at an impact parameter of 2 fm. Solid lines are least square fits to preliminary data (solid symbols) from the E802/E866 Collaboration.

we show the impact parameter dependence of kaon production in Fig. 36. The sensitivity of kaon multiplicity to the impact parameter is at the level of 20% in central collisions, which is rather similar to that of pions. The same level of sensitivity to both the impact parameter and the equation of state in central collisions makes it even harder to learn about the equation of state from these observables. In contrast to the inclusive observables discussed above, collective observables are very sensitive to the equation of state as we shall show in the next section.

F. Baryon transverse flow

Hinted by the findings at Bevelac energies that the collective variables or correlation functions, unlike single-particle observables, are very sensitive to the nuclear equation of state, we now turn to the analysis of the baryon transverse collective flow [63]. Here we use the standard flow analysis in transport models as in Ref. [11]. It has been shown recently in Ref. [64] that an improved flow analysis with the explicit conservation of reaction plane and angular

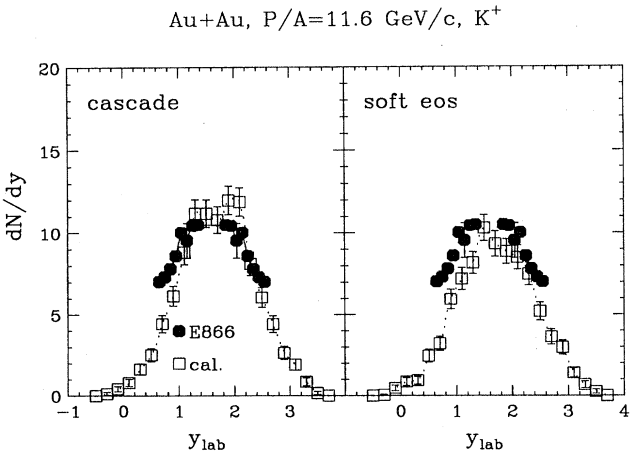

FIG. 35. Rapidity distributions of K^+ in the collision of Au+Au at $P_{\text{beam}}/A = 11.6$ GeV/c at an impact parameter of 2 fm.

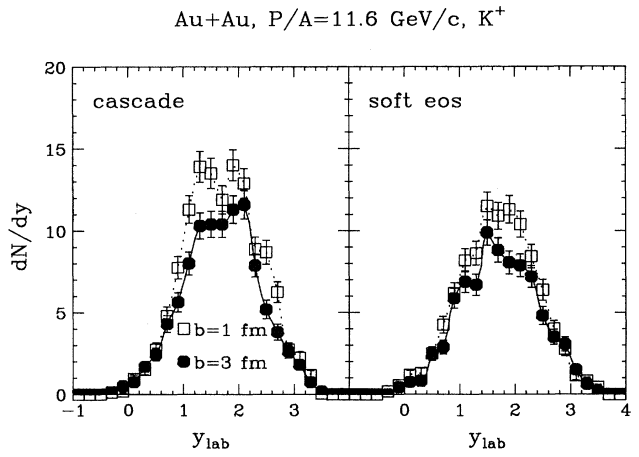

FIG. 36. Comparison of rapidity distributions of K^+ in the collision of Au+Au at $P_{\text{beam}}/A = 11.6$ GeV/c and at impact parameters of 1 and 3 fm.

momentum in an individual hadron-hadron collision results in an increase of the transverse momentum by about 8%–23% at Bevalac energies. This small enhancement is not expected to affect our discussions and conclusions.

First, we show in Fig. 37 the average transverse momentum of nucleons in the reaction plane as a function of rapidity for the collision of Au+Au at $P_{\text{beam}}/A = 11.6$ GeV/c and at impact parameters of 2, 6, and 10 fm. It is seen that the collective flow is the strongest in midcentral collisions in both calculations. Most importantly, significant differences exist between calculations with and without the mean field for collisions at all three impact parameters. In particular, the flow parameter defined as

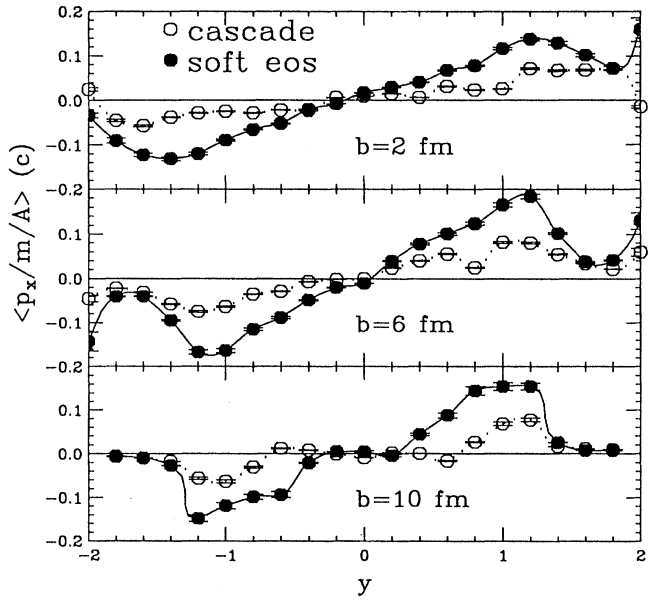

FIG. 37. Baryon average transverse velocity in the reaction plane as a function of rapidity for Au+Au collisions at $P_{\text{beam}}/A = 11.6$ GeV/c and at impact parameters of 2, 6, and 10 fm.

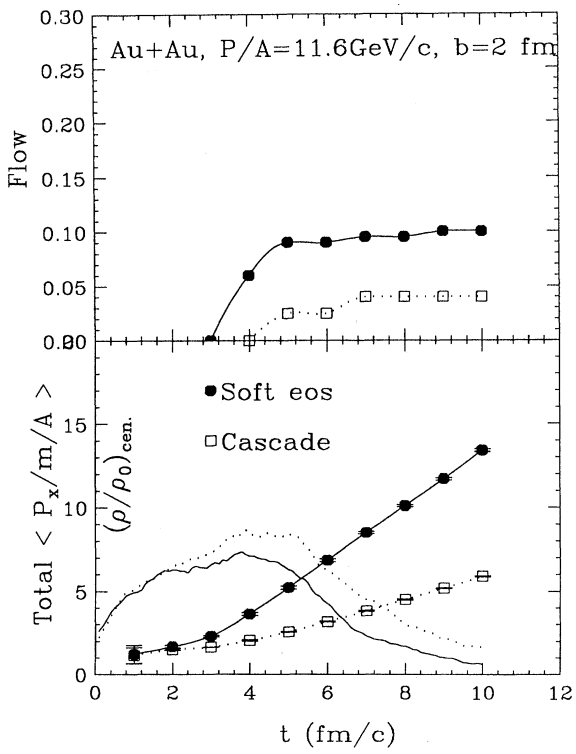

FIG. 38. Time evolution of the flow parameter, the central density, and the total in-plane transverse momentum in the collision of Au+Au at $P_{\text{beam}}/A = 11.6$ GeV/c and at an impact parameter of 2 fm.

$$F = \left\langle \frac{dp_x}{dy} \right\rangle_{y_{\text{c.m.}}} \tag{104}$$

is about a factor of 2.5 larger in the case with the mean field. The strength of the so-called "bounce-off" effect at target or projectile rapidities is also much stronger in calculations with the mean field. To measure the strength of the "bounce-off" effect, we define the average total in-plane transverse momentum as

$$\langle P_x \rangle = \int_{-2}^{2} |dp_x/dy| dy. \tag{105}$$

To see how the collective flow is a sensitive probe of the reaction dynamics in the high density region, we show in Fig. 38 and Fig. 39 the flow parameter F and the total in-plane transverse momentum $\langle P_x \rangle$ as functions of time for Au+Au reactions at impact parameters of 2 fm and 6 fm, respectively. For comparisons, the central densities are also shown in the lower windows of Fig. 38 and Fig. 39. It is clearly seen that the flow is mainly generated in the high density region and does not change in the expansion phase. The increase of the total in-plane transverse momentum during the expansion phase is much more substantial in the case with the mean field than in the cascade case. This indicates that the mean field effect is large in the expansion phase as we have expected. The total in-plane transverse momentum

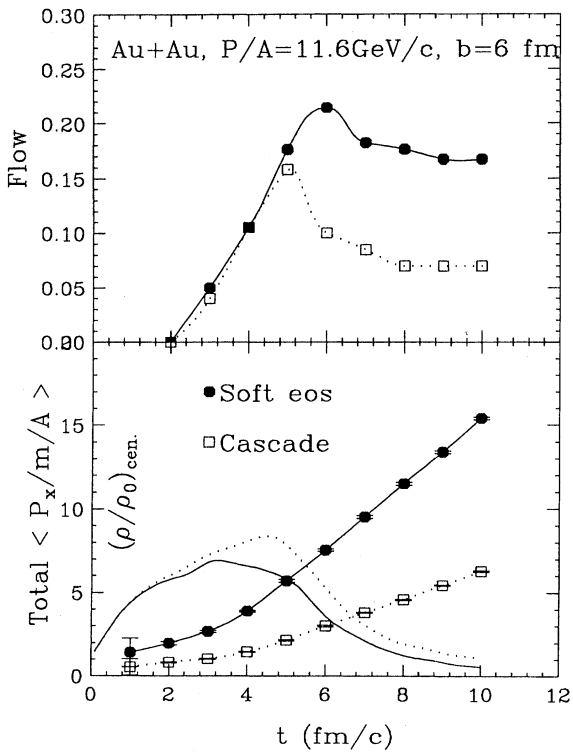

FIG. 39. Same as Fig. 38 at an impact parameter of 6 fm.

reaches its final value after about 15 fm/c. The ratio of final flow parameters in the calculations with and without the mean field is about 2.5 at both impact parameters. This difference is large enough for distinguishing the predictions from different models. For collision at an impact parameter of 6 fm, the flow parameter decreases slightly before reaching its final value. This is mainly due to the reflection of hot baryons from the cold spectator nucleons in collisions at large impact parameters.

It is interesting to note that a clear signature of transverse collective flow has been discovered recently in Au+Au reactions at $p_{\rm beam}/A = 11.4$ GeV/c by the E877 collaboration [65]. In this experiment the distribution of the normalized transverse energy dipole moments is found to shift systematically toward finite values for more central collisions. We are planning to make a detailed comparison with these data in the near future. Furthermore, the preliminary data of the E877 collaboration indicates a smaller transverse momentum in the reaction plane than the predictions from both present and other models [66,67], which may indeed indicate that the equation of state is significantly softened due to the formation of the quark-gluon plasma.

IV. SUMMARY

In summary, we have developed a new relativistic transport model (ART 1.0) for heavy-ion collisions at the AGS energies. This model is an extension of the very successful BUU model for intermediate energy heavy-ion collisions by including more baryon and meson resonances as well as interactions among them. Comparing to the well-known ARC model [3], the present model has more resonances which are found to be important for the collision dynamics and particle production at AGS energies. Moreover, we have used consistently finite mass distributions for these resonances which have significant effects on particle spectra. In addition, a self-consistent mean field for baryons is included. However, comparing to another well-known RQMD model [2], where all resonances up to mass of 2.0 GeV are explicitly included, we do not have as many baryon resonances. Nevertheless, we have partially included the effects of these resonances by using meson+baryon cross sections calculated from the implicit formation of higher resonances. As we are mainly interested in developing a reliable model for energies up to about 15 GeV/nucleon, we do not invoke the string-rope mechanisms for particle production as in RQMD.

Because of the lack of some hadron-hadron collision data, the input to the model still has some uncertainties. Several assumptions used in the model may need to be improved in future versions of the model. In particular, interactions among resonances are largely unknown and have been assumed to be the same as nucleon-nucleon interactions. Additional hadrons, such as $\bar{p}$, $\bar{\Lambda}$, etc., are to be included in the model. At AGS energies the resonance population is as large as that of nucleons in the compression phase, and the assumption of the same mean field for nucleons and resonances may need to be improved. Currently, the finite formation time for produced particles has only been partially taken into account through the finite lifetime of the resonances. A more consistent method may be necessary. Also, it is of interest to include the mean field potential for pions [68,69] and kaons [70] as well as the Bose enhancement factor for pions [71]. The most inconsistent, but also probably the most interesting, feature shared by this model and others is the prediction that the conditions for forming the quark-gluon plasma have already been reached in heavy-ion collisions at AGS energies. In particular, at the maximum baryon density of about $9\rho_0$ and meson density of $4.5\rho_0$ hadrons are squeezed on top of each other and probably melt into the quark-gluon plasma. At this high density hadronic models naturally breaks down. It remains a great challenge to actually include the quark and gluon degrees of freedom into the model and to study the phase transition.

With the above reservations about the validity of the model, we have studied several aspects and issues of heavy-ion reactions at AGS energies. In particular, we have explored effects of the nuclear mean field on the collision dynamics, the formation of superdense hadronic matter, and single-particle observables as well as the radial and transverse collective flow. It is found that the mean field significantly reduces the maximum energy and baryon densities of the superdense hadronic matter formed in the collision. Inclusive single-particle observables are sensitive to the equation of state only at the level of 20%. On the other hand, the transverse collective flow of baryons are found to be very sensitive to the equation of state. In particular, including a soft nuclear equation of state increases the flow parameter by a factor of 2.5 which is large enough to distinguish the pre-

dictions from different theoretical models. Moreover, this sensitivity also indicates that the collective flow can be a useful probe of the formation of the quark-gluon plasma at AGS energies. Preliminary data have shown a smaller baryon transverse flow in the reaction plane than model predictions, and this may indeed indicate the significant softening of the equation of state due to the formation of the quark-gluon plasma. It is very encouraging that the present model has been very useful for studying the interesting physics in high energy heavy-ion collisions.

ACKNOWLEDGMENTS

We would like to thank many participants at the program "Hot and dense nuclear matter" held at the National Institute for Nuclear Theory in Seattle for interesting discussions. In particular, we are indebted to W. Bauer, L.P. Csernai, P. Danielewicz, S. Das Gupta, V. Koch, G.Q. Li, J. Randrup, D. Strottman, and Gy. Wolf for their constructive suggestions and criticisms. This work was supported in part by NSF Grant No. PHY-9212209 and the Welch Foundation Grant No. A-1110.

[1] Proceedings of Heavy Ion Physics at the AGS, HIPAGS'93, 1993, edited by G.S.F. Stephans, S.G. Steadman, and W.L. Kehoe (unpublished); Quark Matter '93 [Nucl. Phys. **A566**, 1c (1994)].

[2] H. Sorge, H. Stöcker, and W. Greiner, Ann. Phys. (N.Y.) **192**, 266 (1989); R. Mattiello, H. Sorge, H. Stöcker, and W. Greiner, Phys. Rev. Lett. **63**, 1459 (1989); H. Sorge, A.V. Keitz, L. Winckelmann, A. Jahns, H. Sorge, H. Stöcker, and W. Greiner, Phys. Lett. B **263**, 353 (1991); M. Hofmann, R. Mattiello, H. Sorge, H. Stöcker, and W. Greiner, Phys. Rev. C **51**, 2095 (1995) and references therein.

[3] Y. Pang, T.J. Schlagel, and S.H. Kahana, Phys. Rev. Lett. **68**, 2743 (1992); T.J. Schlagel, Y. Pang, and S.H. Kahana, *ibid.* **69**, 3290 (1992); S.H. Kahana, Y. Pang, T.J. Schlagel, and C. Dover, Phys. Rev. C **47**, R1356 (1993).

[4] L. Bravina, L.P. Csernai, P. Levai, and D. Strottman, Phys. Rev. C **50**, 2161 (1994), and references therein.

[5] J.I. Kapusta, A.P. Vischer, and R. Venugopalan, Phys. Rev. C **51**, 901 (1995).

[6] E802/E866 Collaboration, F. Videbaek *et al.,* in Proceedings of Quark Matter '95, Monterey, CA, 1995 [Nucl. Phys. **A590**, 249c (1995)].

[7] E877 Collaboration, J. Barrette *et al.,* in Proceedings of Quark Matter '95 [6], p. 259c.

[8] EOS Collaboration, P. Bradly *et al.,* AGS proposal "Exclusive Study of Nuclear Collisions at the AGS," LBL report, 1993.

[9] B.A. Li, C.M. Ko, and G.Q. Li, Report Nucl-th/9502047.

[10] B.A. Li, C.M. Ko, and G.Q. Li, in Proceedings of the 11th Winter Workshop on Nuclear Dynamics, 1995, Key West, Florida, edited by A. Mignery *et al.* (unpublished).

[11] G.F. Bertsch and S. Das Gupta, Phys. Rep. **160**, 189 (1988).

[12] B.A. Li and W. Bauer, Phys. Lett. B **254**, 335 (1991); Phys. Rev. C **44**, 450 (1991).

[13] B.A. Li, W. Bauer, and G.F. Bertsch, Phys. Rev. C **44**, 2095 (1991).

[14] *Total Cross-sections for the Reactions of High Energy Particles*, edited by A. Baldini, V. Flaminio, W.G. Moorhead, and D.R.O. Morrison (Springer-Verlag, Berlin, 1988).

[15] B.J. VerWest and R.A. Arndt, Phys. Rev. C **25**, 1979 (1980).

[16] Gy. Wolf, G. Batko, W. Cassing, and U. Mosel, Nucl. Phys. **A517**, 615 (1990).

[17] P. Danielewicz and G.F. Bertsch, Nucl. Phys. **A533**, 712 (1991).

[18] Gy. Wolf, W. Cassing, and U. Mosel, Nucl. Phys. **A552**, 549 (1993).

[19] S. Huber and J. Aichelin, Nucl. Phys. **A573**, 587 (1994).

[20] B.A. Li, Nucl. Phys. **A552**, 605 (1993).

[21] H.M. Pilkuhn, *Relativistic Particle Physics* (Springer-Verlag, Berlin, 1979).

[22] G.F. Bertsch, M. Gong, L. McLerran, V. Ruuskanen, and E. Sarkkinen, Phys. Rev. D **37**, 1202 (1988).

[23] C.M. Ko, Z.G. Wu, L.H. Xia, and G.E. Brown, Phys. Rev. Lett. **66**, 2577 (1991); Phys. Rev. C **43**, 1881 (1991).

[24] O. Benary, R. Price, and G. Alexander, Berkeley report, 1970.

[25] J. Randrup and C.M. Ko, Nucl. Phys. **A343**, 519 (1980).

[26] K. Tsushima, S.W. Huang, and A. Faessler, Phys. Lett. B **337**, 245 (1994).

[27] J. Cugnon and R.M. Lombard, Nucl. Phys. **A422**, 635 (1984).

[28] G.Q. Li and C.M. Ko, Nucl. Phys. **A** (submitted).

[29] *Properties and Production Spectra of Elementary Particles*, edited by A.N. Diddens, H. Pilkuhn, and K. Schlüpmann (Springer-Verlag, Berlin, 1972).

[30] C.Y. Wong, *Introduction to High Energy Heavy-Ion Collisions* (World Scientific, Singapore, 1994).

[31] C. Grant and J. Kapusta, Phys. Rev. C **32**, 663 (1985).

[32] E. Osnes and D. Strottman, Phys. Lett. **166B**, 5 (1986).

[33] J.N. Ginocchio, Phys. Rev. C **17**, 195 (1978).

[34] M. Baldo and L.S. Ferreira, Nucl. Phys. **A569**, 645 (1994).

[35] M. Betz and T.-S.H. Lee, Phys. Rev. C **23**, 375 (1981).

[36] T.S.-H. Lee and K. Ohta, Phys. Rev. C **25**, 3043 (1982).

[37] B.ter Haar and R. Malfliet, Phys. Rep. **149**, 287 (1987).

[38] H. Esbensen and T.-S.H. Lee, Phys. Rev. C **32**, 1966 (1985).

[39] J.S. O'Connell and R.M. Sealock, Phys. Rev. C **42**, 2290 (1990).

[40] Y. Horikawa, M. Thies, and F. Lenz, Nucl. Phys. **A345**, 386 (1980).

[41] M.B. Johnson and D.J. Ernst, Ann. Phys. (N.Y.) **219**, 266 (1992).

[42] B.A. Li, Phys. Lett. B **292**, 246 (1993); **300**, 14 (1993); Phys. Rev. C **47**, 693 (1993).

[43] B.A. Li, Phys. Lett. B **319**, 412 (1993); Nucl. Phys. **A570**, 797 (1994).

[44] G.E. Brown, Nucl. Phys. **A522**, 397c (1991); G.E. Brown and M. Rho, Phys. Rev. Lett. **66**, 2720 (1991).

[45] D.B. Kaplan and A.E. Nelson, Phys. Lett. B **175**, 57 (1986); A.E. Nelson and D.B. Kaplan, Phys. Lett. B **192**, 193 (1987).

[46] T. Hatsuda and S.H. Lee, Phys. Rev. C **46**, R34 (1992).

[47] M. Asakawa, C.M. Ko, P. Lévai, and X.J. Qiu, Phys. Rev. C **46**, R1159 (1992); M. Asakawa and C.M. Ko, Nucl. Phys. **A560**, 399 (1993).

[48] P. Danielewicz, Phys. Rev. C **51**, 716 (1995).

[49] B.A. Li, C.M. Ko, and G.Q. Li, Phys. Rev. C **50**, R2675 (1994).
[50] D.H. Rischke, H. Stöcker, and W. Greiner, J. Phys. G **14**, 191 (1988); Phys. Rev. D **41**, 111 (1990).
[51] N.K. Glendenning, Nucl. Phys. **A512**, 737 (1990).
[52] M. Gyulassy, in Proceedings of Quark Matter '95 [6], p. 431c.
[53] C.Y. Wong, Phys. Rev. C **25**, 1461 (1982).
[54] P. Braun-Munzinger, J. Stachel, J.P. Wessels, and N. Xu, Phys. Lett. B **333**, 33 (1995).
[55] E802/E866 Collaboration, Michel Gonin, in Proceedings of Heavy-ion Physics at the AGS, 1993, edited by G.S.F. Stephans, S.G. Steadman, and W.L. Kehoe [Nucl. Phys. **A553**, 799c (1993)].
[56] J. Rafelski and B. Müller, Phys. Rev. Lett. **48**, 1066 (1982).
[57] C.M. Ko and L.H. Xia, Phys. Lett. B **222**, 343 (1989).
[58] J. Aichelin and C.M. Ko, Phys. Rev. Lett. **55**, 2661 (1985).
[59] S.W. Huang *et al.*, Phys. Lett. B **298**, 41 (1993).
[60] X.S. Fang, C. M. Ko, G.Q. Li, and Y.M. Zhang, Phys. Rev. C **49**, R608 (1994); Nucl. Phys. **A575**, 766 (1994).
[61] T. Maruyama, W. Cassing, U. Mosel, S. Teis, and K. Weba, Nucl. Phys. **A573**, 653 (1994).
[62] B.A. Li, Phys. Rev. C **50**, 2144 (1994).
[63] P. Danielewicz and G. Odyniec, Phys. Lett. **157B**, 146 (1985).
[64] J. Zhang, S. Das Gupta, and C. Gale, Phys. Rev. C **50**, 1617 (1994).
[65] E877 Collaboration, J. Barrette *et al.,* Phys. Rev. Lett. **73**, 2532 (1994).
[66] J.P. Wessels, in Proceedings of the 11th Winter Workshop on Nuclear Dynamics, 1995, Key West, Florida, edited by A. Mignery *et al.* (unpublished).
[67] E877 Collaboration, Y. Zhang *et al.*, in Proceedings of Quark Matter '95 [6], p. 557c.
[68] L. Xiong, C.M. Ko, and V. Koch, Phys. Rev. C **47**, 788 (1993).
[69] V. Koch and G.F. Bertsch, Nucl. Phys. **A552**, 591 (1993).
[70] G.Q. Li, C.M. Ko, and B.A. Li, Phys. Rev. Lett. **74**, 235 (1995).
[71] G. Welke and G.F. Bertsch, Phys. Rev. C **45**, 1403 (1992); G.F. Bertsch, in *Statistical Description of Transport in Plasma, Astro- and Nuclear Physics*, edited by J. Misquich, G. Pelletier, and P. Schuck (Nova Science Publishers, New York, 1993), p. 337.